



**POLITECNICO**  
MILANO 1863

**[RE.PUBLIC@POLIMI](mailto:RE.PUBLIC@POLIMI)**

Research Publications at Politecnico di Milano

## Post-Print

This is the accepted version of:

G. Droandi, G. Gibertini, D. Grassi, G. Campanardi, C. Liprino  
*Proprotor-Wing Aerodynamic Interaction in the First Stages of Conversion from Helicopter to  
Aeroplane Mode*  
Aerospace Science and Technology, Vol. 58, 2016, p. 116-133  
doi:10.1016/j.ast.2016.08.013

The final publication is available at <http://dx.doi.org/10.1016/j.ast.2016.08.013>

Access to the published version may require subscription.

**When citing this work, cite the original published paper.**

© 2016. This manuscript version is made available under the CC-BY-NC-ND 4.0 license  
<http://creativecommons.org/licenses/by-nc-nd/4.0/>

Permanent link to this version

<http://hdl.handle.net/11311/999101>

# Proprotor-Wing Aerodynamic Interaction in the First Stages of Conversion from Helicopter to Aeroplane Mode

G. Droandi<sup>1,\*</sup>, G. Gibertini<sup>2</sup>, D. Grassi<sup>3</sup>, G. Campanardi<sup>3</sup>, C. Liprino<sup>4</sup>

*Politecnico di Milano, Dipartimento di Scienze e Tecnologie Aerospaziali  
Campus Bovisa, Via La Masa 34, 20156 Milano, Italy*

---

## Abstract

Tiltrotors have the potential to revolutionise air transportation since they combine the flight performance of aeroplanes with the versatility of helicopters. One of the most crucial features characterising tiltrotors is represented by the aerodynamic interaction between wing and rotor. Although this phenomenon has been largely studied using both experiments and calculation, analyses were mainly focused on helicopter operative mode and hovering condition. The present work is aimed at describing the effects due to the aerodynamic interference between wing and rotor of a tiltrotor aircraft employing the tiltwing concept solution during the first stage of the conversion manoeuvre from helicopter to aeroplane configuration. Experimental tests carried out in the open test section of the Politecnico di Milano Large Wind Tunnel with a half-span scaled powered model are reported in detail and results are illustrated in terms of rotor performance and wing aerodynamic loads. Both isolated rotor and half-span model test results are presented as function of several parameters. Overall aircraft performance during the first part of the conversion manoeuvre is finally discussed.

*Keywords:* Aerodynamics, Tiltwing, Tiltrotor, Conversion, Wind Tunnel.

---

---

\*Corresponding author

*Email address:* [giovanni.droandi@polimi.it](mailto:giovanni.droandi@polimi.it) (G. Droandi)

<sup>1</sup>Postdoctoral Fellow

<sup>2</sup>Assistant Professor

<sup>3</sup>Wind Tunnel Engineer

<sup>4</sup>Aeronautical Engineer

## Nomenclature

$A^R$	Rotor disk area, $\pi R^2$ , m <sup>2</sup>
$A^W$	Half-wing surface, $\frac{1}{2}(c_{root}^W + c_{tip}^W)b^W$ , m <sup>2</sup>
$b^W$	Half-wing span, m
$\beta_0$	Coning angle, deg
$c^R$	Rotor blade local chord, m
$c_{root}^W$	Half-wing root chord, m
$c_{tilt}^W$	Half-wing tilt chord, m
$c_{tip}^W$	Half-wing tip chord, m
$c_\infty$	Free stream speed of sound, m/s
$C_{F_x}^R$	Rotor longitudinal force coefficient, $F_x^R / (\rho A^R (\Omega R)^2)$
$C_{F_z}^R$	Rotor vertical force coefficient, $F_z^R / (\rho A^R (\Omega R)^2)$
$C_{F_x}^W$	Half-wing longitudinal force coefficient, $F_x^W / (\frac{1}{2} \rho A^W U_\infty^2)$
$C_{F_z}^W$	Half-wing vertical force coefficient, $F_z^W / (\frac{1}{2} \rho A^W U_\infty^2)$
$C_H$	Rotor drag force coefficient, $H / (\rho \pi \Omega^2 R^4)$
$C_{M_y}^W$	Half-wing pitching moment coefficient, $M_y^W / (\frac{1}{2} \rho A^W c_{tilt}^W U_\infty^2)$
$C_P$	Rotor power coefficient, $P / (\rho \pi \Omega^3 R^5)$
$C_T$	Rotor thrust coefficient, $T / (\rho \pi \Omega^2 R^4)$
$F_{Weight}^A$	Half-aircraft weight, N
$F_x^{FT}$	Half-Fuselage and tail longitudinal force, N
$F_x^N$	Nacelle longitudinal force, N
$F_z^N$	Nacelle vertical force, N
$F_x^R$	Rotor longitudinal force, N
$F_z^R$	Rotor vertical force, N
$F_x^W$	Half-wing longitudinal force, N
$F_z^W$	Half-wing vertical force, N
$M_y^W$	Half-wing pitching moment, N
$M_{Tip}$	Blade tip Mach number, $\Omega R / c_\infty$
$M_\infty$	Free stream Mach number, $U_\infty / c_\infty$
$\mu$	Advance ratio, $U_\infty / \Omega R$
$N_b$	Number of blades
$\Omega$	Angular speed, rad/s
$P$	Rotor power, W

$R$	Rotor radius, m
$\rho$	Air density, kg/m <sup>3</sup>
$\sigma$	Rotor solidity, $cN_b/(\pi R)$
$T$	Rotor thrust, N
$\theta_0$	Collective pitch angle, deg
$\theta_{1c}$	Lateral cyclic pitch angle, deg
$\theta_{1s}$	Longitudinal cyclic pitch angle, deg
$\tau^N$	Nacelle angle of attack, deg
$\tau^W$	Tilting wing angle of attack, deg
$U_\infty$	Free stream velocity, m/s

## 1. Introduction

The idea of an aircraft that would combine the flight performance of modern propeller driven aeroplanes with the versatility and control characteristics of common helicopters has inspired engineers and researchers for decades. One of the most interesting solutions that has the potential to revolutionise the modern air transportation is represented by the tiltrotor [1]. Such a machine is a hybrid configuration aircraft that can alternatively fly like a helicopter and an aeroplane, since it is able to take-off and land vertically and to fly in cruise at high speed. Even though many alternative configurations were investigated, only two were found to be suitable for practical applications. The first configuration is represented by tiltrotor conventional layout, which has two big tilting rotors mounted at the tips of a fixed wing, and the second one is the more complex tiltwing solution, characterised by smaller propellers installed on a tilting wing. Research models such as the XV-3 and XV-15, and commercial aircraft such as the V-22 Osprey and AW609, represent successful designs of conventional tiltrotor [2] while the VZ-2, the XC-142 and the CL-84 are examples of experimental models employing the tiltwing concept [3]. Aeronautical industries, research institutions and universities have investigated tiltrotor and tiltwing concepts for more than forty years, working out most of the basic engineering problems. Recently, the will of bringing such aircraft into commercial service [4] gave a new pulse to the research on this hybrid machine, although several areas require further development and analysis.

As already well known, one of the most important features characterising tiltrotors is represented by the aerodynamic interaction between wing and rotor. Indeed, the rotor wake interference with the wing is mainly responsible for download, unsteady flow separation over lifting surfaces and high vibrations. Many research activities have been devoted to identifying strategies or to designing devices able to reduce the download force acting on the wing of a conventional tiltrotor in hovering and caused by the interaction with the rotor wake [5, 6]. This phenomenon has been broadly investigated using both experiments [7, 8] and calculation

[9]. Even though these studies were mainly focused on helicopter operative mode and hovering condition, further analyses were carried out on both transition manoeuvre [10] and aeroplane operative mode [11].

Among all the conditions belonging to the flight envelop of a tiltrotor, the transition flight regime is probably the most complex one. Indeed, the transition operative mode refers to the conversion manoeuvre from helicopter to aeroplane mode and vice-versa. Conventional tiltrotors, such as XV-15, V-22 Osprey and AW609, accomplished the manoeuvre by rotating nacelle/rotor groups from  $90^\circ$  (vertical position, helicopter mode) to  $0^\circ$  (horizontal position, aeroplane mode). Wing trailing edge flaps and horizontal tail were also used during transition to control the aircraft behaviour. Obviously, the conversion manoeuvre is strongly influenced by rotors since they are responsible for the production of the majority of the lift and propulsive force. Thus, the rotor wake interference with the airframe assumes a central role during the transition flight regime. Some attempts have been made to describe in depth the rotor wake interaction mechanism with a straight wing in forward flight. In these regards, Funk and Komerath [12] used several experimental techniques to capture the primary features of the interaction of a two-bladed rotor wake system with a wing. The same experimental setup was used by Matos et al. [13] to analyse the effects of a deflecting trailing edge flap on rotor/wing interaction.

Transition mode was also studied in the frame of comprehensive wind tunnel test campaigns carried out on full-span powered tiltrotor models. These activities were devoted to investigating performance, stability and control, aircraft loads and rotor wake interaction on the airframe in hover, transition and cruise. For instance, at the beginning of 1970s Boeing conducted a program of four wind tunnel testing campaigns on a motorised model of the Boeing Model 160 [14] to establish design criteria and aerodynamic prediction techniques for tiltrotor concept. A few years later, NASA performed a series of wind tunnel test campaigns on different tiltrotor powered models. In particular a one-fifth length scaled aeroelastic model of the Bell Model 300 tiltrotor aircraft [15] was tested in the Vought Aeronautics Low Speed Wind Tunnel to determine performance, stability and control, and aeroelastic characteristics. On the other hand, a one-tenth length scaled aerodynamically similar model of the Bell Model D-270 tiltrotor aircraft [16] was tested in the NASA-Langley V/STOL wind tunnel to gather useful data for application to the design of existing and future tiltrotor aircraft. In 1980, XV-15 was tested at full-scale in the Ames 40- by 80-foot wind tunnel [17] by NASA in order to determine the aircraft behaviour and to collect data that accurately described the aircraft aerodynamic characteristics. In the late 2000 , a 1/4-scaled powered model of the V-22 Osprey was developed and tested in the Ames 40- by 80-foot wind tunnel [18] in order to achieve a detailed insight in tiltrotor aeromechanics and to generate a comprehensive database for validating analyses.

As part of a European initiative to develop an advanced tiltrotor configuration, the research project ERICA (Enhanced Rotorcraft Innovative Concept Achievement [19]) was proposed by AgustaWestland at the beginning of the 2000s and was funded by the European Community. The main objective of this project was the design of an innovative aircraft for the understanding of an advanced tiltrotor basic phenomena. In

order to overcome drawbacks affecting conventional tiltrotors, such as strong wing/rotor interactions and limited cruise performance, the tiltwing concept [3] was re-introduced using a brand-new wing that can be partially rotated. Although this aircraft configuration was widely studied within several European projects [20, 21], a complete characterisation of the aerodynamic behaviour of the partial tilting wing solution has not been given yet. Actually, a 1/5-scaled full-span motorised model was developed in the frame of the NICETRIP (Novel Innovative Competitive Effective Tilt Rotor Integrated Project) project funded by the European Community. Measurement campaigns were undertaken in the DNW-LLF (German-Dutch Wind Tunnels Large Low-speed Facility) and S1MA ONERA (Office National d'Études et de Recherches Aéropatiales) wind tunnels to test respectively helicopter low speed configurations [22] and high speed aeroplane configurations [23]. Nevertheless, the aerodynamic database gathered during the aforementioned activities is not public. Furthermore, only few data related to the ERICA conversion manoeuvre was published on scientific literature. In particular, literature presents a lack of experimental data regarding this manoeuvre for a thorough assessment of the aircraft performance and for the validation of both computational fluid dynamics (CFD) and computational structural dynamics (CSD) models. As a consequence, an in depth analysis of the conversion manoeuvre of a tiltrotor with a partially tilting wing would broaden the knowledge on this kind of aircraft and would be very helpful for future designs.

In the present paper, the effects due to the aerodynamic interference between wing and rotor of a tiltrotor aircraft employing the tiltwing solution were investigated during the first stage of the transition manoeuvre that allows the aircraft to convert from the helicopter to the aeroplane configuration. For this purpose, a tiltwing aircraft representative of a new generation V/STOL aircraft in the same class of ERICA was considered. The aircraft was designed to be a civil passenger transportation aircraft able to carry a maximum of 22 passengers with luggage and was characterised by a pair of small diameter, wingtip mounted proprotors and a partially tilting wing. A description of the aircraft can be found in Droandi's doctoral dissertation [24]. A wind tunnel half-span powered model of the reference tiltwing aircraft was designed and manufactured at the Department of Aerospace Science and Technology (DAER) Aerodynamic Laboratory [25, 26]. A comprehensive experimental campaign focused on the hovering flight condition, including forces and flow field measurements, was conducted by the authors [27, 28] to study the effects of the partially tilting wing solution on the overall aircraft performance. Experimental data and numerical results confirmed the effectiveness of the tilting wing solution for download alleviation maintaining good aircraft performance in hover. The purpose of the present work is to further improve the knowledge on the aerodynamic behaviour of a tiltwing by providing a useful description of the effects related to the aerodynamic interaction between a partially tilting wing and the rotor wake system during the first steps of the conversion manoeuvre. In the following sections the test rig and the measurement procedure are described in detail and measured rotor and wing airloads are presented as function of several parameters, such as nacelle angle of attack, tilting wing angle of attack, advance ratio and rotor thrust. Both isolated rotor and half-span model test results

are discussed and finally the overall aircraft performance is deduced.

## 2. Wind tunnel tests

A tiltwing was designed to be a civil passenger transportation aircraft able to carry a maximum payload of 2200 kg which corresponds to a maximum of 22 passengers with luggage. The aircraft was designed to be representative of a new V/STOL aircraft belonging to the same class of the civil tiltrotor ERICA. The aircraft was characterised by a partially tilting wing with a span of 15 m and a pair of small diameter, wingtip mounted proprotors having a diameter of 7.4 m (dimensions are given at full-scale). A more detailed description of the full-scale aircraft can be found in Droandi's doctoral dissertation [24].

In order to investigate the aerodynamic interaction between wing and rotors, a wind tunnel half-span model of the tiltwing aircraft considered was designed and manufactured at the DAER Aerodynamic Laboratory. Experimental tests were carried out in the open test section of the Politecnico di Milano Large Wind Tunnel (GVPM). The GVPM is an atmospheric closed loop wind tunnel, with a test section of 4 m  $\times$  3.84 m. The maximum wind velocity achievable is 55 m/s and the turbulence intensity is of the order of 0.1 %.

In the following, the experimental test rig and the tiltwing half-span model are described and the experimental test conditions are discussed.

### 2.1. Experimental test rig

The wind tunnel half-span model of the reference tiltwing aircraft was designed to represent one rotor, the nacelle (the air-intake was not reproduced) and the corresponding half-wing. A sketch of the experimental test rig installed in the open test section of the GVPM is reported in Figure 1. The overall dimensions of the open test section and the distances of the rotor model from the wind tunnel convergent and diffuser are reported in Figure 1. The aircraft fuselage was not reproduced in the experimental model because its influence on the rotor wake flow was very small and could be considered negligible, as the rotor radius of a tiltwing aircraft was considerably smaller than conventional tiltrotor (as for instance the V-22 or the BA-609). In order to measure the rotor and the wing loads separately, the nacelle/rotor system was designed to be independent from the half-wing system. This solution also allowed to test alternatively the isolated rotor and the half-span model. Furthermore, the experimental rig design permitted to test the model both in hovering [27] and during the first stage of the conversion manoeuvre. A geometrical scale of 1/4 with respect to the full-scale aircraft was used to design the wind tunnel model. As a consequence, the model rotor radius was  $R = 0.925$  m and the span of the half-wing was  $1.90 R$ . Table 1 summarises important geometrical dimensions of the wind tunnel tiltwing half-span model.

Figure 2 shows the tiltwing half-span model in the open test section of the GVPM during the conversion tests. The four bladed rotor hub was placed at a height of  $5 R$  from the ground and was located on a

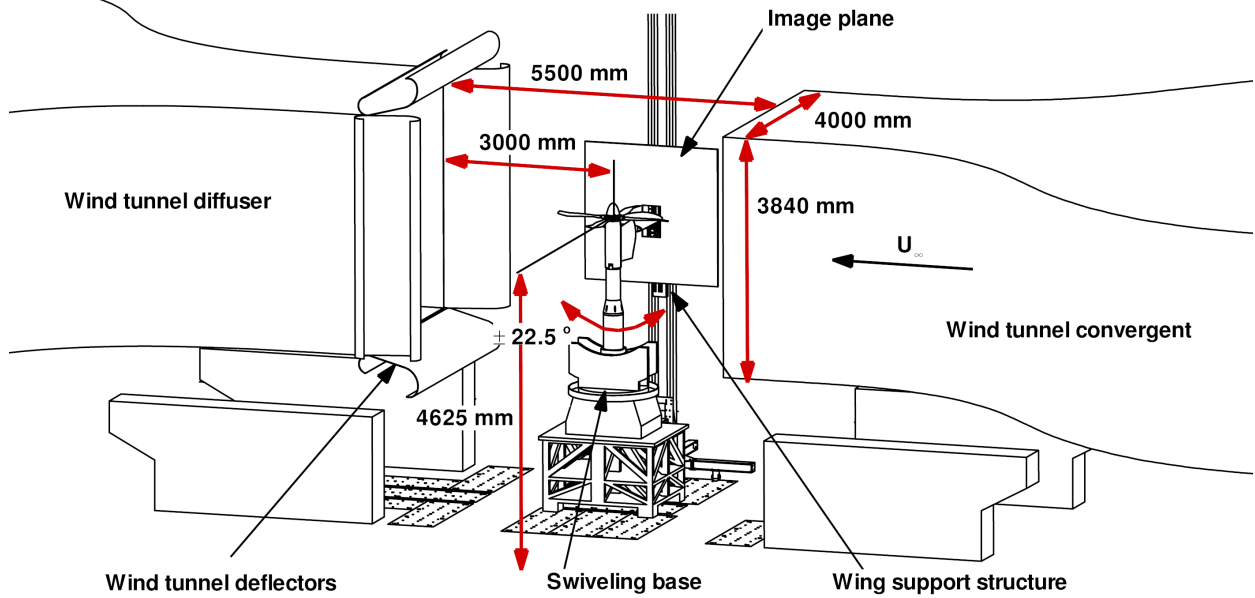


Figure 1: Sketch of the experimental setup.

Number of blades	4
Rotor radius	0.925 m
Rotor disk area	2.688 m <sup>2</sup>
Rotor solidity	0.192
Nacelle maximum radius	0.250 m
Nacelle height (without hub)	0.750 m
Half-wing span	1.758 m
Half-wing root chord	0.750 m
Half-wing tilt section chord	0.625 m
Half-wing tip chord	0.520 m
Fixed half-wing portion span	0.933 m
Half-wing surface	1.114 m <sup>2</sup>
Wing airfoil	NACA 64A221
Wing rotation axis / rotor disk distance	0.430 m
Image plane	2.035 × 2.035 m

Table 1: Wind tunnel half-span model geometrical details.

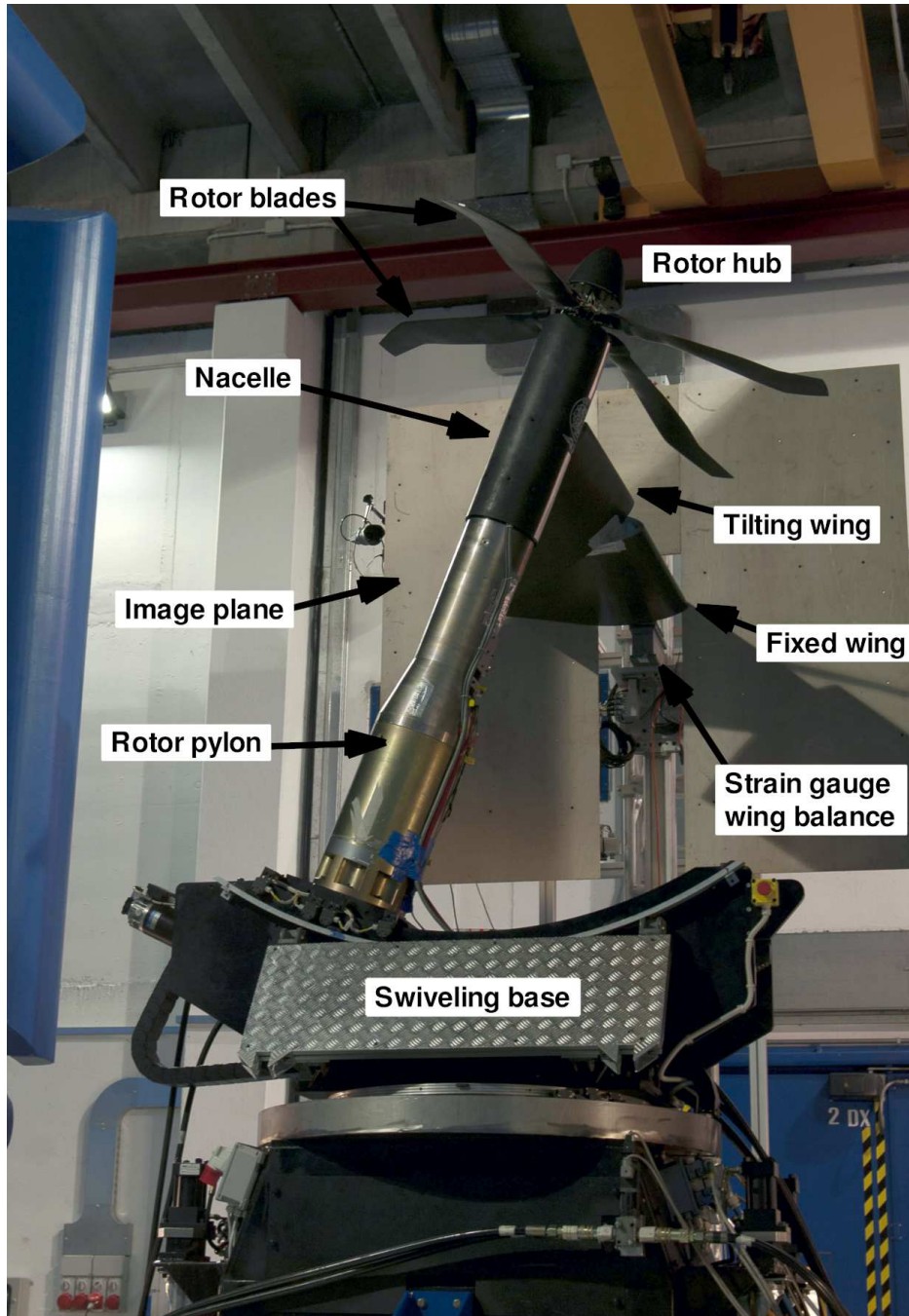


Figure 2: The tiltwing half-span model in the open test section of the Politecnico di Milano Large Wind Tunnel.

strut which was composed of an aluminium base (not visible in Figure 2), a swivelling base and a rigid pylon. The swivelling base allowed to rotate the pylon and the rotor hub about the rotor hub centre. Such degree of freedom (maximum angular displacement achievable of  $22.5^\circ$  both backwards and forwards with respect to the vertical direction) enabled to change the nacelle angle of attack ( $\tau^N$ ) keeping unchanged the

distance between the rotor hub centre and the ground. The rotor shaft transferred the drive torque from the hydraulic motor (maximum power 16 kW at 3000 rpm), placed inside the swivelling base (not visible in Figure 2), to the rotor blades. The loads produced by the rotor were measured by a six-component strain gauge hollow balance (2000 N FS vertical force, accuracy 0.25 % FS) mounted below the rotor hub. The torque was measured by an instrumented shaft passing through the balance and joined to the transmission shaft by a torsionally stiff steel laminae coupling. The whole system was checked using reference weights, and a maximum error of 0.5 N was found.

The rotor rotational speed was measured by a Hall effect sensor that was also used to trigger the data acquisition with respect to the azimuthal position of a selected blade (named in the following as master blade). The azimuthal reference position ( $\psi = 0^\circ$ ) corresponded to the position assumed by the master blade when it was pointing towards the aircraft tail. The rotor was equipped with four blades designed in-house [29, 25] and had a thrust-weighted solidity ( $\sigma$ ) of 0.192. In Figure 3 the non-linear chord, twist and sweep distributions are reported along the blade span together with the different airfoils employed. Although tiltrotor aircraft usually employed gimbaled rotor hub to prevent dynamic instabilities that may occur in cruise flight at high-speed (as the whirl flutter instability [30]), the four bladed rotor model available at DAER Aerodynamic Laboratory was a typical fully articulated helicopter rotor hub. Nevertheless, since the tiltwing experimental model was designed to study only conditions with zero or quite low forward flight speed (respectively the hovering condition and the initial part of the conversion manoeuvre from helicopter to aeroplane configuration), it could be reasonably assumed that the hub design did not influence the rotor aerodynamics. As a consequence, the behaviour of a typical tiltrotor gimbaled rotor hub could be assumed to be indistinguishable with respect to a classical helicopter fully articulated rotor head.

Collective, longitudinal and lateral pitch controls were remotely provided to the rotor hub by the swash-plate that is controlled by three independent electric actuators. Mechanical flap and lead-lag hinges allowed the blades to flap and lead or lag with respect to the rotor hub and, together with the pitch hinge, they allowed the blade to move with a prescribed kinematics. The flap hinge was located at a distance of 3.2 % R from the rotor hub axis while the lead-lag hinge had an offset of 5.4 % R with respect to the same axis. No dampers were fitted on the lead-lag hinges of the rotor model. The feathering bearing and the blade cuff were placed outboard of the lead-lag hinge. The blade could be rotated around the feathering axis by the pitch horn that was attached to the blade cuff outboard of the pitch bearing. The connection between the pitch horn and the pitch link lay on the flap hinge axis ensuring no pitch-flap coupling. High accuracy Hall effect sensors and small magnets (diameter 2 mm) were employed on each blade hinge to simultaneously measure flap, lead-lag and pitch angles during the tests. Hall effect sensors had a ratiometric output voltage which varied proportionally with the strength of the magnetic field produced by the magnets. Sensors calibration was carried out *in situ* only once all sensors and all magnets were placed in their final position in order to avoid any modification of the magnetic fields produced by each magnet. The calibration procedure was

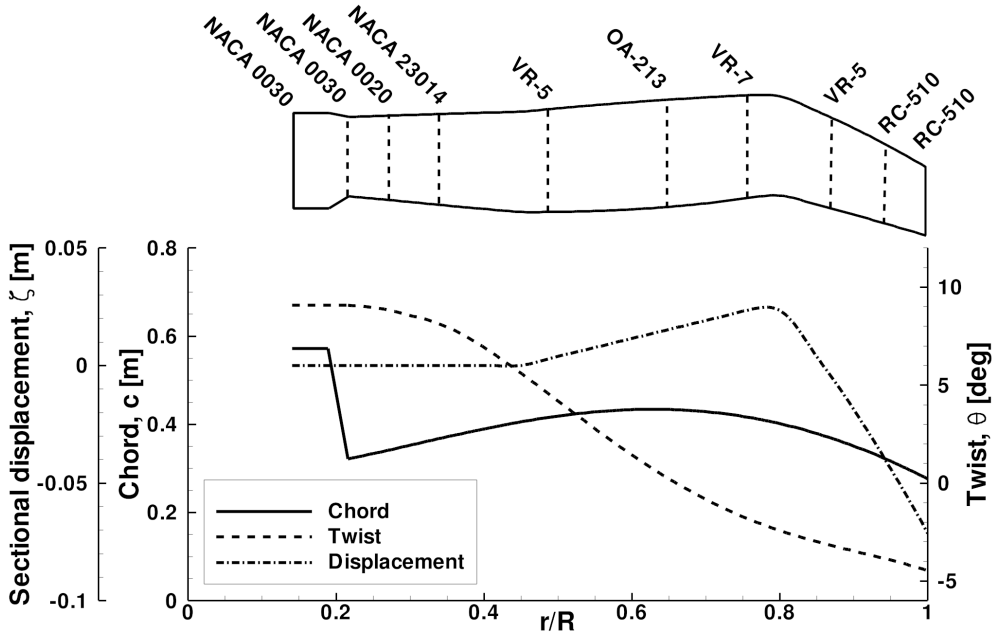
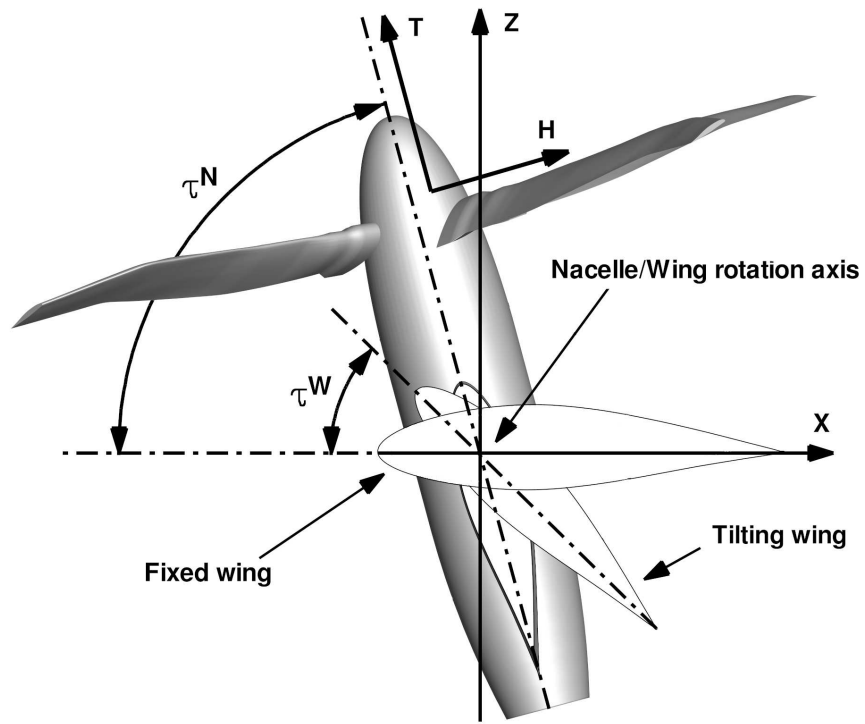


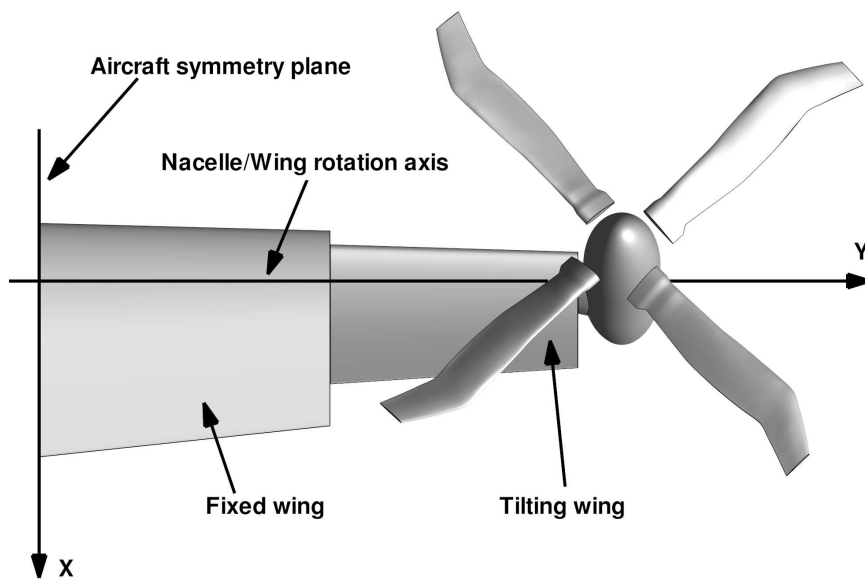
Figure 3: Blade geometry: span-wise distributions of chord, twist, sectional displacement and airfoil.

performed one hinge at a time by fixing the other two hinges in their neutral position and was repeated for each blade. Note that pitch and flap sensors were calibrated using an inclinometer (calibration range: pitch  $[-10^\circ, +22^\circ]$ , flap  $[-4^\circ, +10^\circ]$ ) placed on the blade cuff while the calibration of the lead-lag sensors was carried out using an optical method (calibration range: lead-lag  $[-16^\circ, +8^\circ]$ ). The error on the Hall effect sensors was evaluated as the maximum of the standard deviation with respect to the calibration curves. For pitch and flap sensors this value corresponded to  $0.1^\circ$  while for the lead-lag sensors it was  $1^\circ$ .

The half-wing system was composed of the aircraft half-wing and an image plane. The half-wing was tapered, untwisted and unswept and all the wing sections were aligned with respect to the 25 % of the local chord. The half-span model geometry is illustrated in Figure 4 together with the aircraft reference system, the nacelle  $\tau^N$  and the tilting wing  $\tau^W$  geometrical angles of attack. The axis passing through these points corresponded to the wing rotational axis, as sketched in Figure 4, so that the outer wing portion could be easily rotated about the rotational axis by  $15^\circ$  steps. The half-wing model had a whole span of  $1.90 R$  and represented both fixed and tilting wing portions. The root section of the fixed part of the wing lay on the aircraft symmetry plane while the wing tip section was placed at the nacelle-wing junction. The tilting wing tip was kept separated from the nacelle (the gap was 4 mm long) thus no forces were transmitted between the two sub-systems. The global aerodynamic loads acting on the half-wing model were acquired by a six-component strain gauge balance that was placed at the half-wing root, behind the aircraft symmetry plane. The relative distance between the wing rotational axis and the rotor hub ( $h/R$ ) was 0.465 and was kept



(a) Lateral view



(b) Top view

Figure 4: Sketch of the fixed/tilting wing and rotor and aircraft reference system.

constant during all the tests presented in this paper (this value corresponded to the  $h/R$  design value [27]). In order to achieve a more detailed insight on the phenomena related to the wing/rotor interaction, surface tufts were used to visually examine the flow on the upper surface of the outer part of the wing. Wool tufts were distributed on 5 parallel rows containing 9 tufts each and were fixed on the wing surface using a thin tape. The first row was placed at 25 % of the wing local chord while the last one was placed at the trailing edge. A high-resolution camera located on the symmetry plane behind the wing trailing edge was used to record moving pictures of tuft patterns.

Finally, a squared wooden plane was placed in correspondence of the half-wing root section and was fixed to the wing support with the attempt of reproducing the full-span aircraft behaviour. Such image plane was already employed to test the tiltwing half-span model in hovering condition, as described by Droandi et al. [28]. As already known, for hovering tests of half-span conventional tiltrotor models, the image plane approximation is not correct, as discussed by Polak et al. [31]. Nevertheless, even though in hover condition an image plane may significantly modify the rotor wake boundaries [32] and the velocity field in the fountain flow region [9], it allows to correctly evaluate the global wing and rotor loads and thus the aircraft performance [33, 8]. Furthermore, in the present case the interference effect between the rotor wake and symmetry plane would be smaller with respect to conventional tiltrotor models (for instance XV-15, V-22 Osprey and AW609) because the rotor diameter of the tiltwing aircraft was smaller and thus the distance between blade tip and the symmetry plane was considerably higher. In general, the combined half-span model and image plane solution was often adopted in wind tunnel testing activities [34] to study aircraft wing aerodynamics yielding accurate pitch, lift and downwash estimates. During the past years, this testing solution was also employed for tiltrotor forward flight tests. Recent examples are represented by the free-wing tilt-propeller model [35] tested both in the LTV (Ling Temco Vought) and in the AARL (U.S. Army Aeronautical Research Laboratory) facilities, the TILTAERO (TILTrotor interactional AEROdynamics, [20]) project for the ERICA tests carried out at DNW (German-Dutch Wind Tunnel) and the QTR (Quad TiltRorot [36]) project for the QTR flight demonstrator configuration performed at NASA Langley Transonic Dynamic Tunnel.

## *2.2. Operative conditions*

The aim of the present study was a fundamental investigation on the main aerodynamic phenomena involved in the transition manoeuvre of a tiltwing. Indeed, the purpose of the experimental activity was to highlight possible interference effects arising from the wing/rotor interaction during the conversion and not to reproduce some conditions belonging to the conversion manoeuvre of a specific aircraft. In these regards, a reasonable test matrix was defined taking into account the conversion manoeuvre of both XV-15 [2] and ERICA [22] tiltrotors and neglecting unrealistic test configurations. In Figure 5 the trim conditions tested at GVPM are illustrated and compared with those tested at DNW in the frame of the low forward

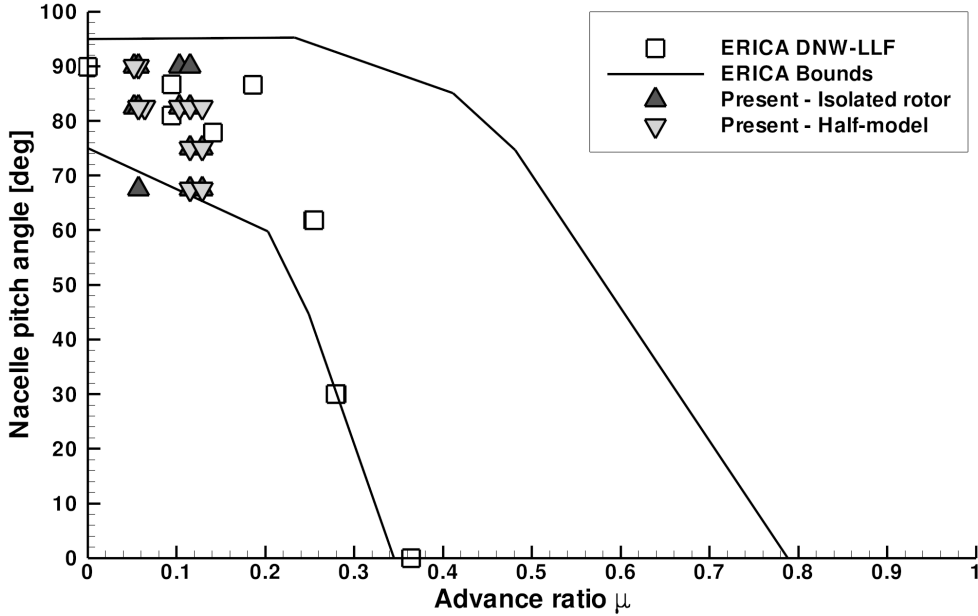


Figure 5: Isolated rotor and half-span model test conditions at GVPM and ERICA flight envelope and test conditions at DNW [22].

speed tests of the NICETRIP project [22]. The test conditions with the nacelle angle of attack equal  $90^\circ$  in forward flight did not represent real flight conditions, nevertheless they were included in the test matrix as a limit case of the rotor/wing interaction.

The experimental tests performed at GVPM consisted in rotor thrust sweeps (the thrust variation is obtained by controlling the collective pitch angle) carried out at a certain setting of nacelle incidence  $\tau^N$ , tilting wing incidence  $\tau^W$ , advance ratio  $\mu$  and keeping the fixed part of the wing at zero angle of attack. During tests, the rotor was controlled by the swashplate and it was manually trimmed by means of an analogical control console at each prescribed collective pitch angle to avoid the flapping motion (i.e. zero one per-rev flapping), as usually done in wind tunnel tests of helicopter rotor models [37, 38]. The diffuser wind tunnel deflectors position for the open jet configuration was  $15^\circ$  of incidence with respect to the wind tunnel diffuser walls, as illustrated in Figure 1. The wind tunnel free stream velocity  $U_\infty$  and the rotor angular velocity  $\Omega$  were set together in order to achieve the required advance ratio, also taking into account test rig mechanical limitations. In particular, the power given by the motor was limited by the hydraulic engine capacity, therefore the rotational speed of the rotor was reduced with respect to the value used for hovering tests to produce reasonable thrust values. In hover, the nominal tip Mach number ( $M_{Tip} = 0.32$  corresponding to 1120 rpm) was imposed to obtain 1/2 the tip Mach number of full-scale aircraft [27]. Forward flight tests in helicopter mode were carried out at slightly lower tip Mach numbers (the rotor rotational speed ranged from a minimum of 800 rpm to a maximum of 1000 rpm). Additionally, in order

to stay within safety wing structural limits, the wind tunnel free stream velocity was limited ( $V_\infty = 5$  m/s and 10 m/s). The aforementioned rotor and wind tunnel operative conditions, that led to an advance ratio ranging from 0.052 to 0.129, have not allowed to keep any Mach or Reynolds numbers similarity with respect to full-scale conditions. A similar scaling strategy was adopted by Marr et al. [16] to select proper scale parameters for the wind tunnel powered model of the Bell Model D-270 tiltrotor. Such a model was used to determine aircraft performance and rotor wake interaction on the airframe in hovering, conversion and cruise flight conditions. In particular, the blade tip Mach number employed to test the one-tenth scaled model during the conversion manoeuvre was 0.37. Such a value was quite similar to the one used in the present work and corresponded to 1/2 the tip Mach number used by the full-scale Bell Model D-270 tiltrotor during conversion.

Nevertheless, important Mach number effects in hovering were limited to the rotor blade tip region and produced very small effects on the rotor wake system [5, 32]. The same conclusions were drawn by Droandi and Gibertini [25], who compared experimental data ( $M_{Tip} = 0.32$ ) and CFD simulations ( $M_{Tip} = 0.32$  and 0.64) of the isolated hovering rotor, finding no relevant differences in terms of performance between different tip Mach numbers. For instance, at  $C_T$  equal 0.0215 the difference in terms of rotor power coefficient obtained at both tip Mach numbers was in the order of 0.4 %. Since the rotor operative conditions selected for forward flight tests were very close to the one previously employed for hovering tests and since the advance ratios tested were small, it could be assumed that Mach number effects were very small on the advancing blade so that wind tunnel results could correctly reproduce the rotor performance. At the same time, Reynolds number effects were not expected to strongly affect the wing behaviour. Indeed, the Reynolds number based on the wing mean chord and the lowest wind tunnel free stream velocity was of the order of  $1.5 \cdot 10^5$ . This value is large enough to not expect important effects on the fixed wing portion at zero angle of attack. On the other hand, the transition of boundary layer on the tilting wing surface was mainly triggered by the rotor wake disturbance, as already observed by Funk and Komerath [12], so that no Reynolds number effects were expected on it.

### *2.3. Data acquisition and reduction*

All the forward flight tests, that consisted in rotor thrust sweeps at constant advance ratio  $\mu$ , were performed using the same test procedure. In more detail, during each run the wind tunnel free stream velocity  $U_\infty$  and the rotor rotational speed  $\Omega$  were remotely adjusted to keep the selected advance ratio  $\mu$  constant. A computer-based acquisition system was used to monitor the tests and to acquire both model and wind tunnel transducers signals. During each thrust sweep, the signals acquisition of each measurement point scheduled took place over a period of 5 s. The acquisition frequency used to simultaneously acquire all the signals was 2.5 kHz. All acquired data was post-processed by keeping the time average of each signal. Blade pitching and flapping motions were also analysed as the Fourier series of rotor hub Hall effect sensors

with respect to the master blade position. Actually, only the pitching motion presented non-zero higher order terms since the blade flapping motion was prevented during the test.

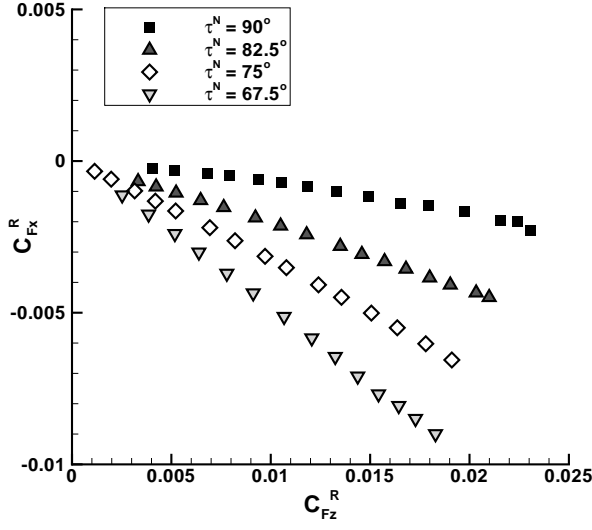
Rotor and wing static forces and moments were computed with respect to the aircraft reference system. As shown in Figure 4, the aircraft reference system was centred at the intersection between the nacelle/wing rotational axis and the aircraft symmetry plane. The  $X$ -axis was aligned with the chord of the fixed wing root and directed toward the wing trailing edge. The  $Y$ -axis corresponded to the wing rotational axis and was directed from the aircraft symmetry plane toward the nacelle. The  $Z$ -axis was then defined according to the right hand rule. Both rotor and wing reference quantities were used to obtain non-dimensional coefficients from dimensional forces and moments. No corrections were applied to rotor and wing static forces and moments for rotor pylon, wing strut and wind-tunnel effects. In fact, although test conditions allowed for rotor measurements to be corrected using the Heyson method [39] and the wing model size allowed for classical wind tunnel corrections [34], the complex tiltwing aircraft geometry having rotor and wing interacting with each other did not permit to apply such classical corrections. The authors are aware that, in principle, the interaction between the rotor wake and the inlet of the wind tunnel diffuser could produce remarkable disturbances that may alter the measurements on the model. In these regards, a qualitative analysis of the flow inside the open test section of the GVPM in presence of an isolated rotor was carried out by Vigevano and Biava [40] using CFD calculation. Numerical results highlighted that the flow field computed with the rotor in the open test section appeared to be qualitatively similar to the flow field calculated in free-flight conditions. However, quantitative effects on the rotor performance can be expected in an intermediate range of flow speeds and rotor thrusts where the rotor wake impinges on the lower deflector of the wind tunnel diffuser. Such a problem would never occur in the present experiment since the selected test conditions were outside the aforementioned range.

### 3. Results and discussion

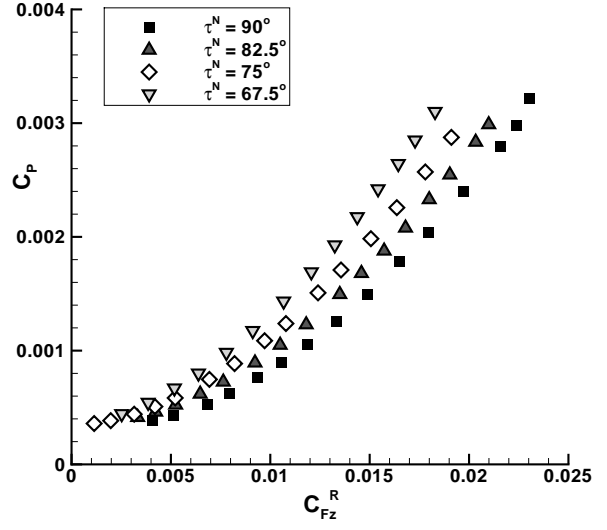
Wind tunnel data gathered at GVPM during the experimental tests are reported and discussed in this section. Firstly, the isolated rotor performance is discussed and both nacelle angle and advance ratio effects are investigated. Secondly, the half-span model results are presented in terms of rotor performance and wing aerodynamic loads. The effects produced by the presence of the wing on the rotor and the influence of the rotor wake system on the wing are analysed in detail. Finally, wind tunnel data was used to deduce the whole aircraft performance in the first stage of the conversion manoeuvre mainly in terms of aircraft lift and drag capabilities.

#### 3.1. Isolated rotor analysis

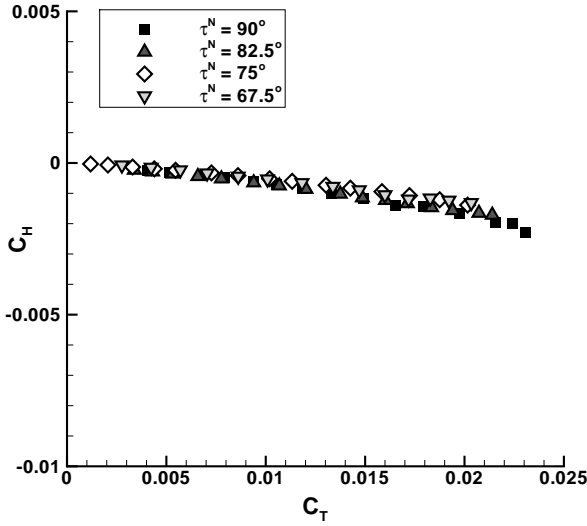
The isolated rotor tests allowed to characterise the rotor blades performance during the initial part of the conversion manoeuvre neglecting the wing effects. Such tests were conducted accounting for different



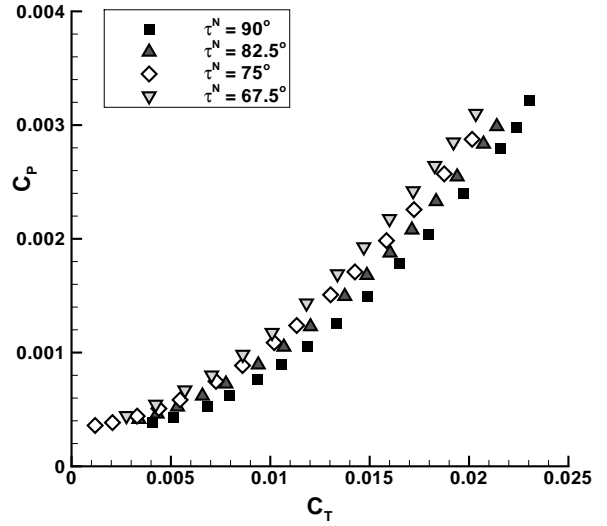
(a) Rotor longitudinal force coefficient



(b) Rotor power coefficient



(c) Rotor drag force coefficient



(d) Rotor power coefficient

Figure 6: Isolated rotor a) longitudinal force coefficient  $C_{Fx}^R$  and b) power coefficient  $C_p$  as function of vertical force coefficient  $C_{Fz}^R$  and rotor c) drag force coefficient  $C_H$  and d) power coefficient  $C_p$  as function of the isolated rotor thrust coefficient  $C_T$  at  $\mu = 0.115$  for different shaft angles.

nacelle angles of attack ( $\tau^N = 90^\circ, 82.5^\circ, 75^\circ$  and  $67.5^\circ$ ) and several advance ratio ( $\mu$  ranging from 0.052 to 0.129). Since all tests were carried out with no blade flapping motion, the rotor tip path plane remained always normal to the rotor rotational axis and consequently the thrust force developed by the rotor was aligned with its axis. The highest nacelle angle of attack ( $\tau^N = 90^\circ$ ) tested during the experiments lay just below the upper boundary of the nacelle pitch angle envelope (see Figure 5) and corresponded to the

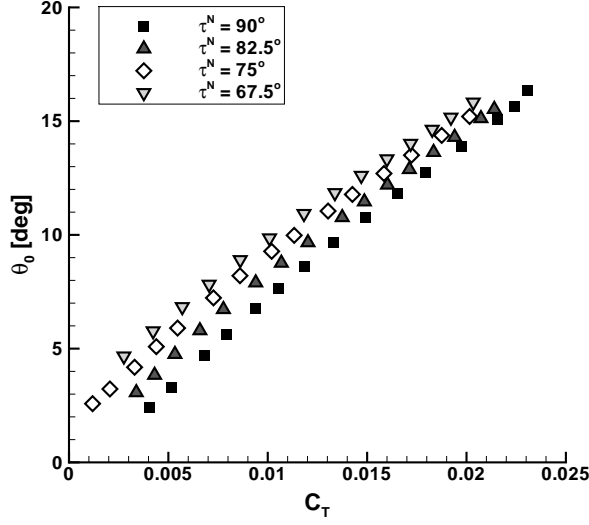
configuration assumed by the rotor in hovering flight in helicopter mode.

Experimental measurements on the isolated rotor revealed that both the rotor performance and its kinematics were strongly influenced by the nacelle angle of attack  $\tau^N$ . Figure 6(a) and 6(b) show respectively the longitudinal force and power coefficients as functions of the rotor vertical force coefficient for an advance ratio  $\mu$  equal to 0.115. In both pictures, the comparison between different nacelle angles of attack  $\tau^N$  is reported. According to the aircraft reference system, negative values of the rotor longitudinal force coefficient  $C_{F_x}^R$  corresponded to a propulsive effect generated by the rotor. As expected, in forward flight conditions the rotor longitudinal force component was always a propulsive force. Furthermore, the lower the nacelle angle of attack the higher the propulsive effect given by the rotor. As shown in Figure 6(a), the relationship between the rotor longitudinal and vertical force coefficients was almost linear. The power required by the rotor to develop a certain amount of vertical force increased as the nacelle angle of attack decreased, as illustrated in Figure 6(b). For example at  $C_{F_z}^R = 0.018$ , power increases of about 13 %, 27 % and 47 % were found respectively at  $\tau^N = 82.5^\circ$ ,  $75^\circ$  and  $67.5^\circ$  with respect to the reference condition having  $\tau^N = 90^\circ$ .

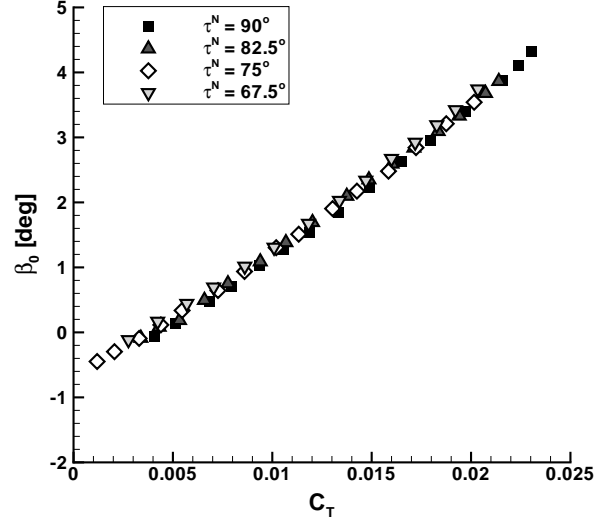
In order to highlight the rotor behaviour, in Figure 6(c) and 6(d) the rotor drag force coefficient  $C_H$ , representing the rotor drag force component defined in the rotor hub plane, and the rotor power coefficient  $C_P$  are shown as function of the rotor thrust coefficient  $C_T$  at various nacelle angles of attack  $\tau^N$ . As already observed for the longitudinal force, negative values of drag force component indicated a propulsive effect. The effects due to the nacelle angle of attack as well as the values of the drag coefficient (see Figure 6(c)) were smaller compared to those observed in terms of longitudinal force component  $C_{F_z}^R$ . The comparison between different shaft angles also highlighted a different trend with respect to Figure 6(a) since, in this case, the lower the  $\tau^N$ , the higher the drag force in the hub plane given by the rotor. For instance at  $C_T = 0.020$ , an increase of about 24 % in the rotor drag was found when  $\tau^N = 67.5^\circ$  with respect to the case having  $\tau^N = 90^\circ$ . A small influence of the shaft angle could also be observed in Figure 6(d) where the power coefficient was directly plotted against the rotor thrust.

The accuracy of the rotor system was evaluated as the maximum values of the standard deviation of thrust and power coefficients that were equal to  $1.08 \times 10^{-4}$  and  $1.35 \times 10^{-5}$  respectively. The standard deviation was evaluated in hovering condition with an imposed trim condition ( $\theta_0 = 12.0^\circ$ ,  $\beta_0 = 2.5^\circ$ ) on the basis of 40 measurements repetitions [28].

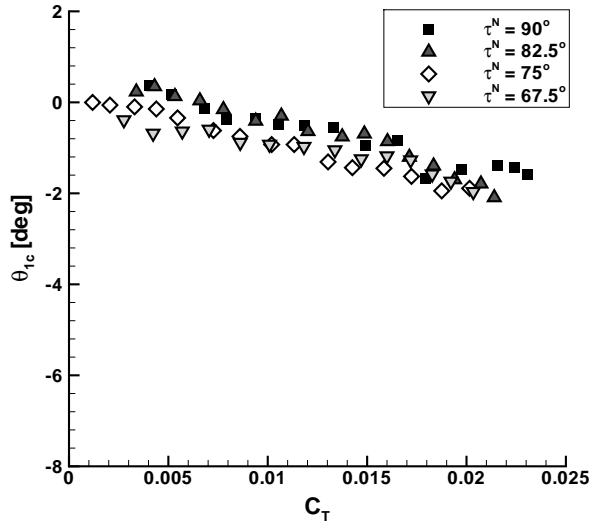
The nacelle angle of attack  $\tau^N$  also strongly influenced the rotor kinematics and thus the rotor trim parameters. Indeed, for a fixed advance ratio  $\mu$ , different values of blade collective pitch angle  $\theta_0$  and lateral and longitudinal cyclic pitch angles  $\theta_{1c}$  and  $\theta_{1s}$  were required to develop the same thrust coefficient at different nacelle angles of attack. In these regards, Figure 7 illustrates the behaviour of the rotor thrust coefficient  $C_T$ , the blade coning angle  $\beta_0$  and the lateral and longitudinal cyclic pitch angles  $\theta_{1c}$  and  $\theta_{1s}$  as function of the rotor thrust coefficient  $\theta_0$ . In particular, as shown in Figure 7(a) for  $\mu = 0.115$ , a decrease of  $7.5^\circ$  of  $\tau^N$  led  $\theta_0$  to an increase of about  $1^\circ$  when  $C_T$  is 0.01 and of about  $0.5^\circ$  when  $C_T$  is 0.02. As



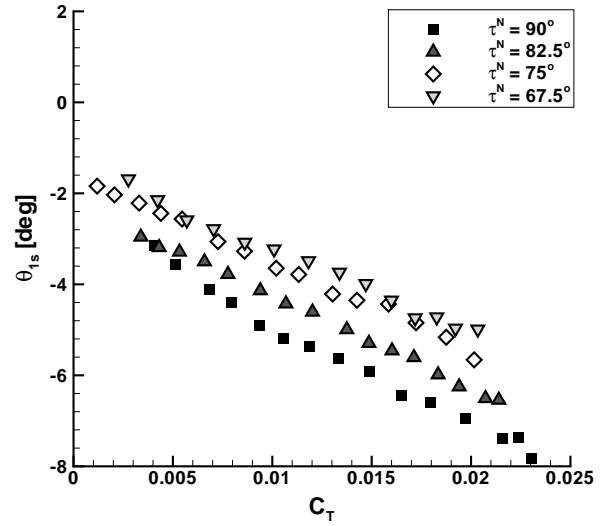
(a) Collective angle



(b) Coning angle



(c) Lateral cyclic pitch



(d) Longitudinal cyclic pitch

Figure 7: Isolated rotor a) collective angle  $\theta_0$ , b) coning angle  $\beta_0$ , c) lateral cyclic pitch angle  $\theta_{1c}$  and d) longitudinal cyclic pitch angle  $\theta_{1s}$  as function of the rotor thrust coefficient  $C_T$  at  $\mu = 0.115$  for different shaft angles.

expected, the lateral cyclic pitch control ranging from  $0^\circ$  to  $-2^\circ$  was slightly affected by the nacelle angle of attack (see Figure 7(c)). On the other hand, as shown in Figure 7(d) the longitudinal cyclic pitch control was significantly influenced by the nacelle angle of attack so that the higher  $\tau^N$  the lower  $\theta_{1s}$ . The nacelle angle of attack did not affect the blade coning angle  $\beta_0$  (see Figure 7(b)). The maximum difference observed at the same thrust coefficient between  $\tau^N$  equal  $90^\circ$  and  $67.5^\circ$  was in the order of  $0.1^\circ$ .

In order to complete the isolated rotor performance analysis, the effects of the advance ratio  $\mu$  were

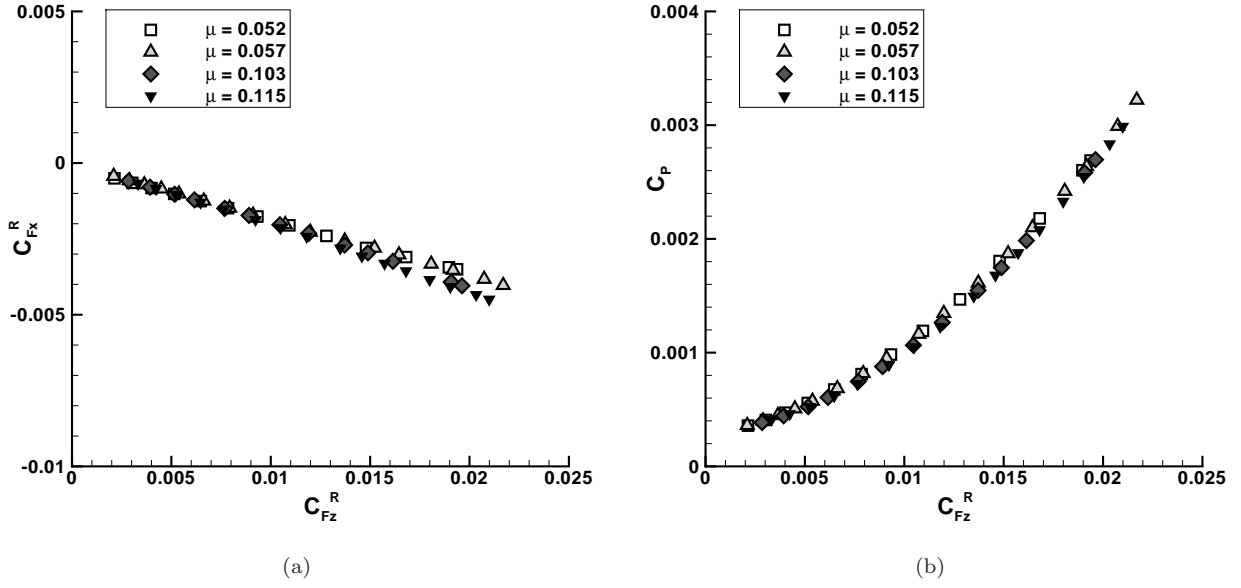


Figure 8: Isolated rotor a) longitudinal force coefficient  $C_{F_x}^R$  and b) power coefficient  $C_P$  as function of vertical force coefficient  $C_{F_z}^R$  at  $\tau^N = 82.5^\circ$  for different advance ratio.

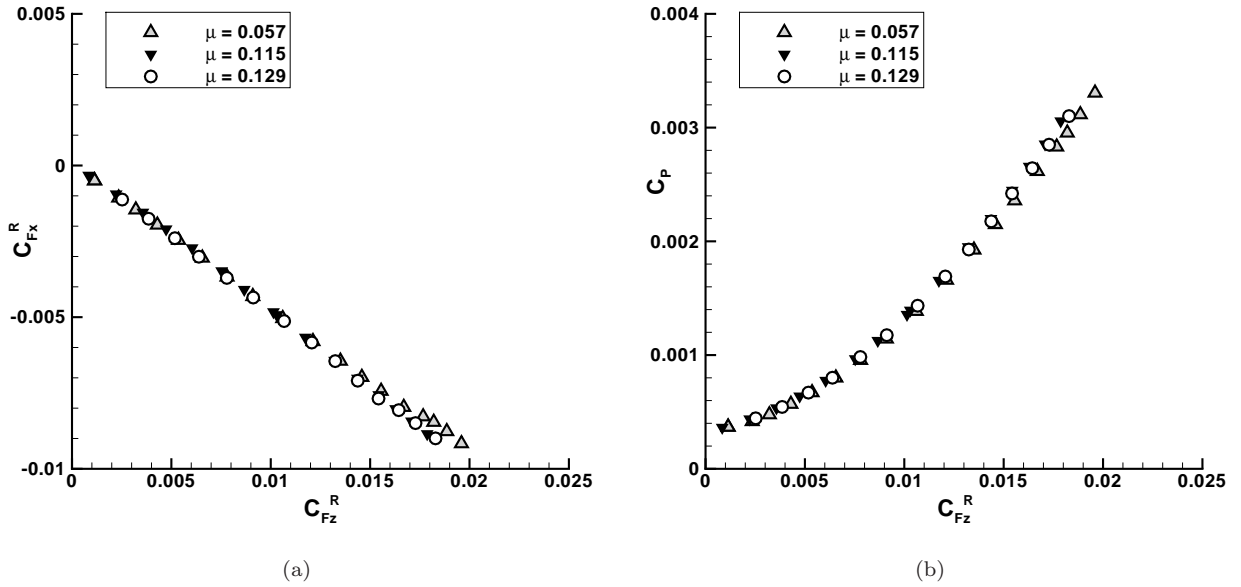


Figure 9: Isolated rotor a) longitudinal force coefficient  $C_{F_x}^R$  and b) power coefficient  $C_P$  as function of vertical force coefficient  $C_{F_z}^R$  at  $\tau^N = 67.5^\circ$  for different advance ratio.

investigated at constant nacelle angle of attack. The comparisons between the longitudinal force and power coefficients as function of the vertical force coefficient are reported in Figure 8 and 9 for two different nacelle angles of attack ( $\tau^N = 82.5^\circ$  and  $67.5^\circ$ ). Actually, the advance ratios analysed during the tests assumed

small values within a limited range. As a result, the advance ratio produced very small effects on rotor performance regardless of the nacelle angle of attack value, as clearly visible in Figure 8 and 9.

### 3.2. Half-span model analysis

The main goal of the wind tunnel measurements on the half-span model was to carry out an in depth study on the mutual interference between rotor and wing of a tiltwing aircraft during the conversion manoeuvre from helicopter to aeroplane configuration. The experimental tests were performed taking into account a combination of different parameters such as the nacelle angle of attack, the advance ratio and the tilting wing angle ( $\tau^W$ ). This approach allowed to investigate several feasible aircraft configurations representative of the tiltwing tiltrotor in the first stage of the conversion corridor, from helicopter configuration having  $\tau^N = 90^\circ$  to low forward speed in conversion configuration having  $\tau^N = 67.5^\circ$ . In particular, tests were performed considering the same values of nacelle angle of attack and advance ratio already analysed for the isolated rotor case. The aerodynamic interference between wing and rotor was studied analysing the effects of different tilting wing angles on rotor performance and evaluating the effects of the rotor slipstream on wing aerodynamic loads.

The analysis of rotor airloads demonstrated that in forward flight conditions the effect produced by the wing on the rotor itself was very small independently of the wing configuration. In more detail, it was found that the tilting wing angle  $\tau^W$  did not affect the rotor performance, as illustrated in Figure 10 for the case at  $\mu = 0.115$  and  $\tau^N = 75^\circ$ . Indeed, rotor longitudinal force and power coefficients measured with different

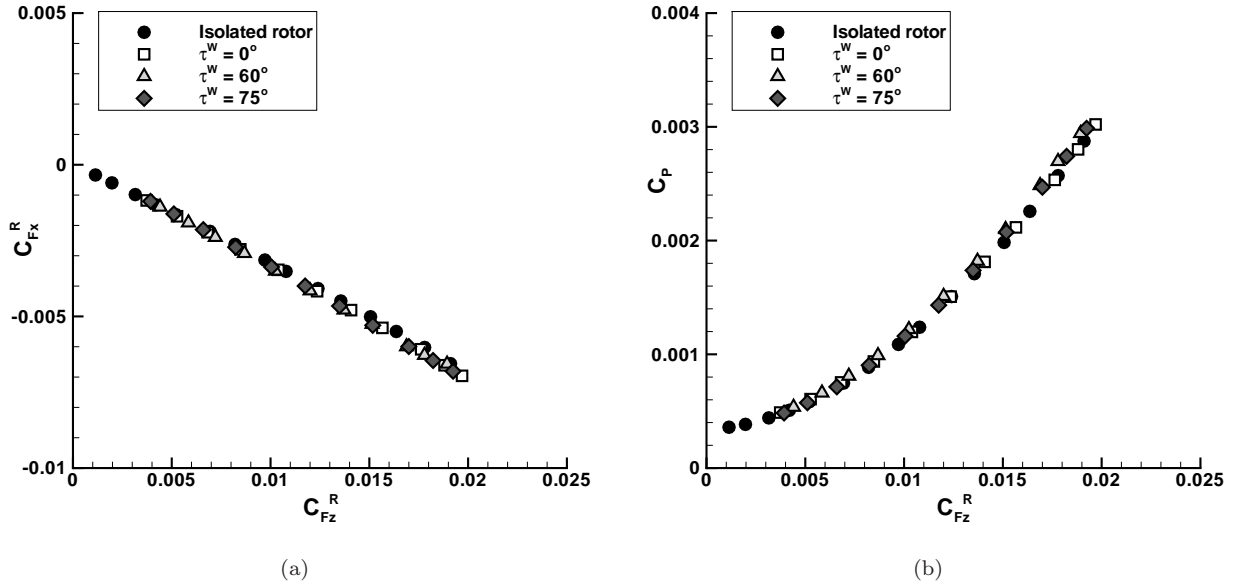


Figure 10: Comparison between isolated rotor and half-span model: a) rotor longitudinal force coefficient  $C_{Fx}^R$  and b) rotor power coefficient  $C_P$  as function of rotor vertical force coefficient  $C_{Fz}^R$  for different tilting wing angle ( $\tau^N = 75.0^\circ$ ,  $\mu = 0.115$ ).

wing configurations (for the case reported in Figure 10,  $\tau^W$  was alternatively set equal to  $75^\circ$ ,  $60^\circ$  and  $0^\circ$ ) were very similar to each other and to the isolated rotor values. Similar results were found for all the configurations tested. This result, obtained at low forward speeds (up to  $\mu = 0.129$ ) and corresponding to very low forward Mach numbers (up to  $M_\infty = 0.03$ ), highlighted that in such conditions the rotor overall performance was not influenced by the presence of the wing or by the configuration of its outer portion. Hall effect sensors measurements on rotor blades revealed that the wing produced small but non-negligible

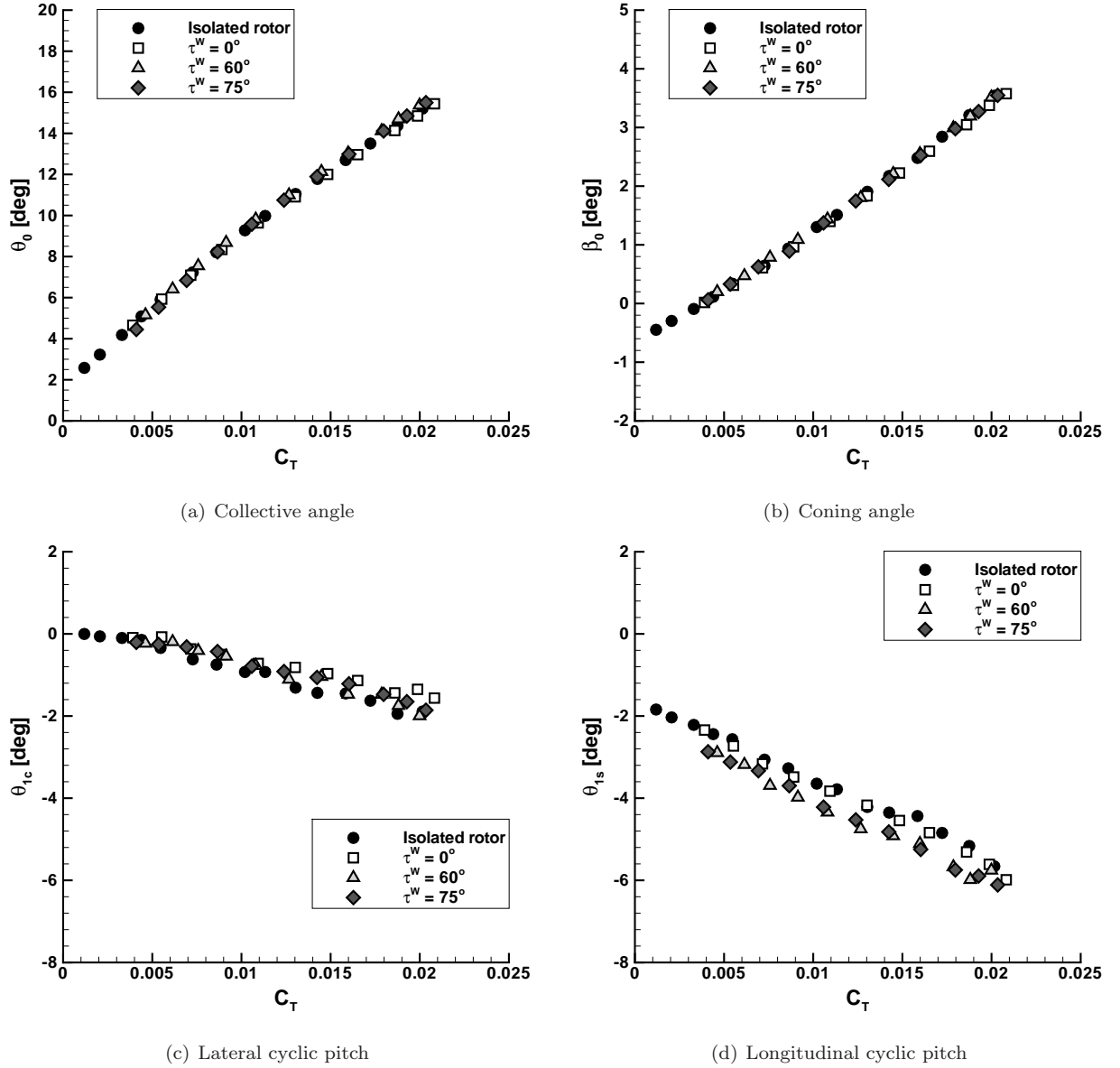


Figure 11: Comparison between isolated rotor and half-span model: a) collective angle  $\theta_0$  b) coning angle  $\beta_0$  c) lateral cyclic pitch angle  $\theta_{1c}$  and d) longitudinal cyclic pitch angle  $\theta_{1s}$  as function of the rotor thrust coefficient  $C_T$  for different tilting wing angle ( $\tau^N = 75.0^\circ$ ,  $\mu = 0.115$ ).

effects on rotor kinematics with respect to the isolated rotor, as depicted in Figure 11. Actually, Figure 11(a) and 11(b) show that both collective and coning angles measured with  $\mu = 0.115$  and  $\tau^N = 75^\circ$  were not influenced by the wing and its configuration. On the other hand, small changes were observed on lateral cyclic while the effects produced by the wing are apparent on longitudinal cyclic. Figure 11(c) and 11(d) compare lateral and longitudinal cyclic pitch controls measured with different tilting wing configurations for the case at  $\mu = 0.115$  and  $\tau^N = 75^\circ$ . In particular, a rather constant decrease of the order of  $0.6^\circ$  with respect to the isolated rotor case was found for the longitudinal cyclic  $\theta_{1s}$  when high angles of attack were imposed to the tilting wing portion. This effect was not observed when the tilting wing part was set at  $\tau^W = 0^\circ$ .

It is well known that wing aerodynamic loads are strongly influenced by the interaction with the rotor wake. In forward flight in helicopter mode, as well as during transition, the interaction mechanism between rotor and wing is usually more complex than in hovering flight and is mainly controlled by the advance ratio. Indeed, in such flight regime, the incoming flow transports the rotor wake behind and below the rotor itself. The behaviour of the rotor wake and the magnitude of its deflection strictly depend on several parameters [38], such as the rotor thrust, the advance ratio and eventually the rotor/airframe interference. Experimental observations on rotor wake geometry carried out by Leishman and Bagai [41] using the wide-field shadowgraph method on an isolated rotor in forward flight showed that the higher the advance ratio, the higher the wake deflection. Even though such measurements demonstrated that considerations based on simple momentum theory tend to overpredict the magnitude of the wake deflection [38], the rotor wake can be considered relatively flat for advance ratios higher than 0.2 [37]. As a consequence, low advance ratios lead to small wake deflections allowing the rotor slipstream to impinge on the wing surface. In this regard, wind tunnel measurements on the one-tenth scaled Bell Model D-270 powered model [16] revealed the influence of rotor slipstream on wing airloads at low advance ratio. However, experimental data showed that wing lift was not influenced by rotor wake above  $\mu = 0.16$ . Beyond this value the wake deflection became big enough so that it no longer interacts with the wing. At low advance ratio ( $\mu = 0.075$ ) the vortex structure released by the blade tip impinged on the upper surface of the wing (placed at  $0^\circ$  of incidence) triggering flow separation and reattachment, as described by Funk and Komerath [12] for a generic tiltrotor having a conventional wing configuration. In such flight condition, the resulting wing download could be reduced by making use of trailing edge flaps that modified the pressure distribution over the wing surface [13].

In a tiltwing, the interference mechanism described above is further affected by the tilting wing configuration ( $\tau^W$ ). This feature was already analysed by Droandi et al. [28] for hovering flight showing that different  $\tau^W$  values produce different aerodynamic loads on the wing. In the transition flight regime the combined effects of rotor induced velocity, free stream velocity, nacelle angle of attack and tilting wing configuration have a strong influence on the local angle of attack of the outer wing portion and consequently on

the airloads of the whole wing. Present results confirmed that the aircraft trim condition has a remarkable influence on wing airloads, at least in the range of advance ratios ( $0.052 \leq \mu \leq 0.129$ ) and nacelle angles ( $90^\circ \leq \tau^N \leq 67.5^\circ$ ) tested. Wing airloads are reported for various nacelle angles and advance ratios in Figure 12, 13 and 14, showing respectively the vertical and longitudinal force coefficients and the pitching moment coefficient as function of rotor vertical force coefficient. The maximum value of the standard deviation of the vertical and longitudinal force coefficients were respectively equal to  $3.9 \times 10^{-3}$  and  $5.1 \times 10^{-3}$ , while it was  $6.6 \times 10^{-3}$  for the pitching moment coefficient. For each combination of  $\tau^N$  and  $\mu$ , different suitable wing configurations were investigated. As shown in pictures, the rotor wake influenced the wing behaviour in all the aircraft configurations tested, and wing airloads changed as the rotor thrust increased.

For  $\mu = 0.052$  and  $\tau^N = 90^\circ$  measurements were carried out with the tilting wing placed alternatively at  $90^\circ$  and  $75^\circ$  of incidence. The latter configuration produced higher vertical force (lift) and lower longitudinal force (drag) than the first one, as can be observed in Figure 12(a) 13(a). The wing vertical force component presented a rather constant behaviour as the rotor vertical force increased. The wing vertical force coefficient obtained with the nacelle at  $75^\circ$  of incidence was higher than the case with  $\tau^W = 90^\circ$ , resulting in a difference of 0.31 at  $C_{Fz}^R = 0.020$ . For very small values of rotor vertical force, the wing longitudinal force coefficient was of the order of 1.5 when  $\tau^W = 90^\circ$  and 1.2 when  $\tau^W = 75^\circ$ , as depicted in Figure 13(a). It is interesting to observe that these values are similar to the drag of a flat plate having the same height-to-span ratio as the outer wing portion, placed at  $90^\circ$  of incidence with respect to the free stream and at the same Reynolds number (in this condition, a reasonable drag value for a flat plate is 1.18, see for example Hoerner [42]). This result confirmed that for very small rotor thrust values, the effect of the rotor wake on the wing was almost negligible. When the rotor thrust increased, the rotor aerodynamic interaction with the wing caused a substantial increase of both longitudinal force and pitching moment, as illustrated in Figure 13(a) and 14(a). Highest values of  $C_{Fx}^W$  and  $C_{My}^W$  were obtained with the nacelle placed at  $90^\circ$ . In such configuration, the maximum wing longitudinal force coefficient measured during the experiments was 4.01 at  $C_{Fz}^R = 0.02$  with respect to 2.42 obtained at  $75^\circ$ , while the maximum pitching moment coefficient was 0.92 instead of 0.54.

As expected, the wing behaviour was strongly modified when changing the nacelle angle from  $90^\circ$  to another incidence. Measurements carried out at nacelle angles lower than  $90^\circ$  of incidence showed that both vertical and longitudinal wing force components increased as the rotor thrust increased. Such a behaviour, observed for high tilting wing angles of incidence, proved that the interaction mechanism between rotor wake and wing was responsible for improving the wing performance during the first part of the transition manoeuvre since the wing vertical force component increased much more than the longitudinal force component.

Figures 12(b), 13(b) and 14(b) compare the results obtained for two different tilting wing incidences ( $\tau^W = 75^\circ$  and  $60^\circ$ ) at  $\mu = 0.115$  and  $\tau^N = 82.5^\circ$ . In such conditions, both wing configurations exhibited

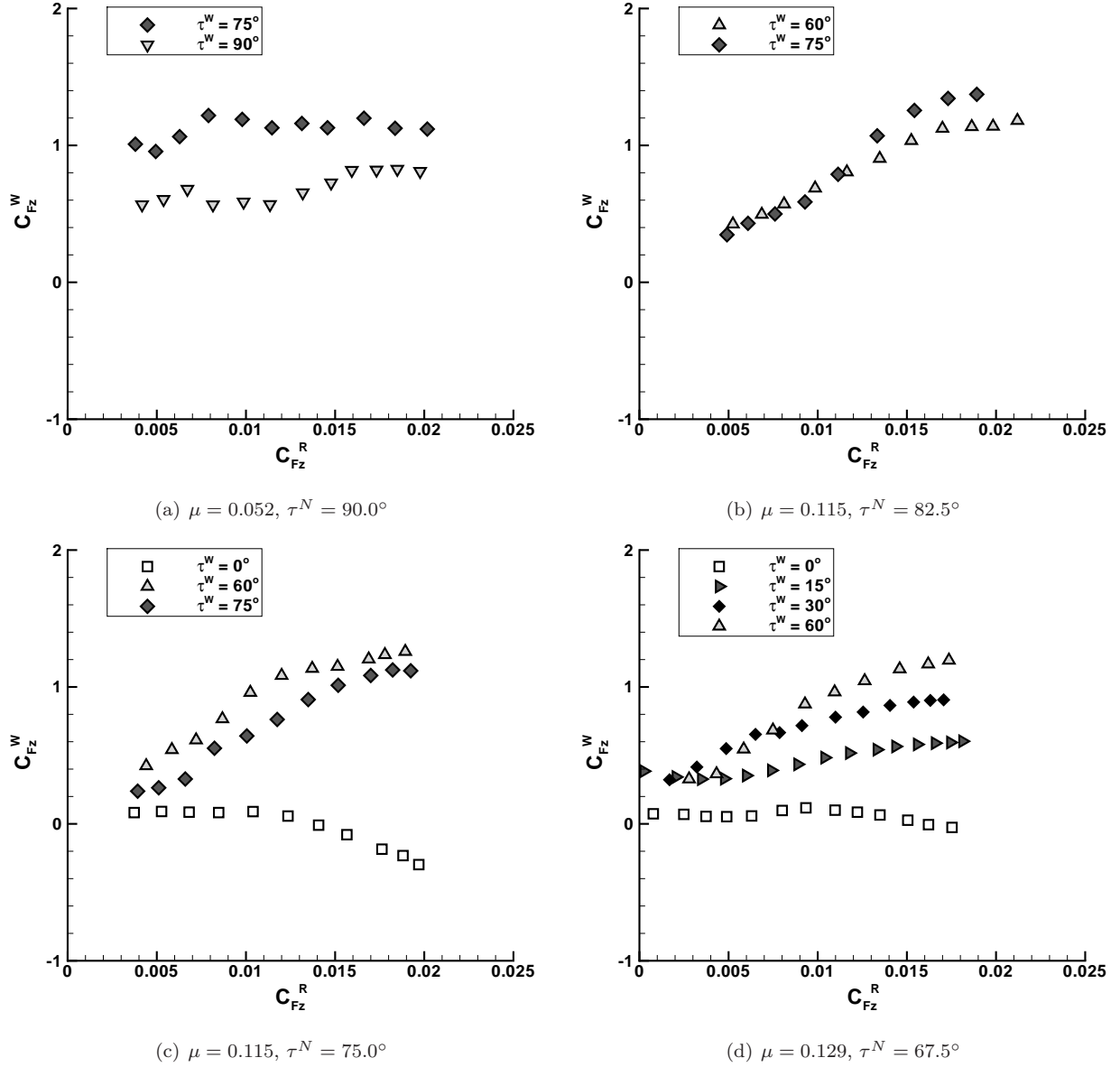


Figure 12: Wing vertical force coefficient  $C_{Fz}^W$  as function of rotor vertical force coefficient  $C_{Fz}^R$  for the half-span model configuration. Comparison between different tilting wing angle  $\tau^W$  for different advance ratios and nacelle angles.

good aerodynamic performance, although the tilting wing was set at very high angles of attack with respect to the free-stream velocity. Indeed, when changing the nacelle angle from  $90^\circ$  to  $82.5^\circ$  of incidence, both  $C_{Fx}^W$  and  $C_{My}^W$  values strongly decreased with respect to the previous case while  $Fz^W$  reached similar values as before. This interesting result was mainly due to the rotor/wing aerodynamic interaction mechanism that positively influenced the wing behaviour. Indeed, the actual angle of attack seen by the tilting wing was strongly reduced with respect to its geometrical incidence ( $\tau^W$ ) since the velocity distribution around the

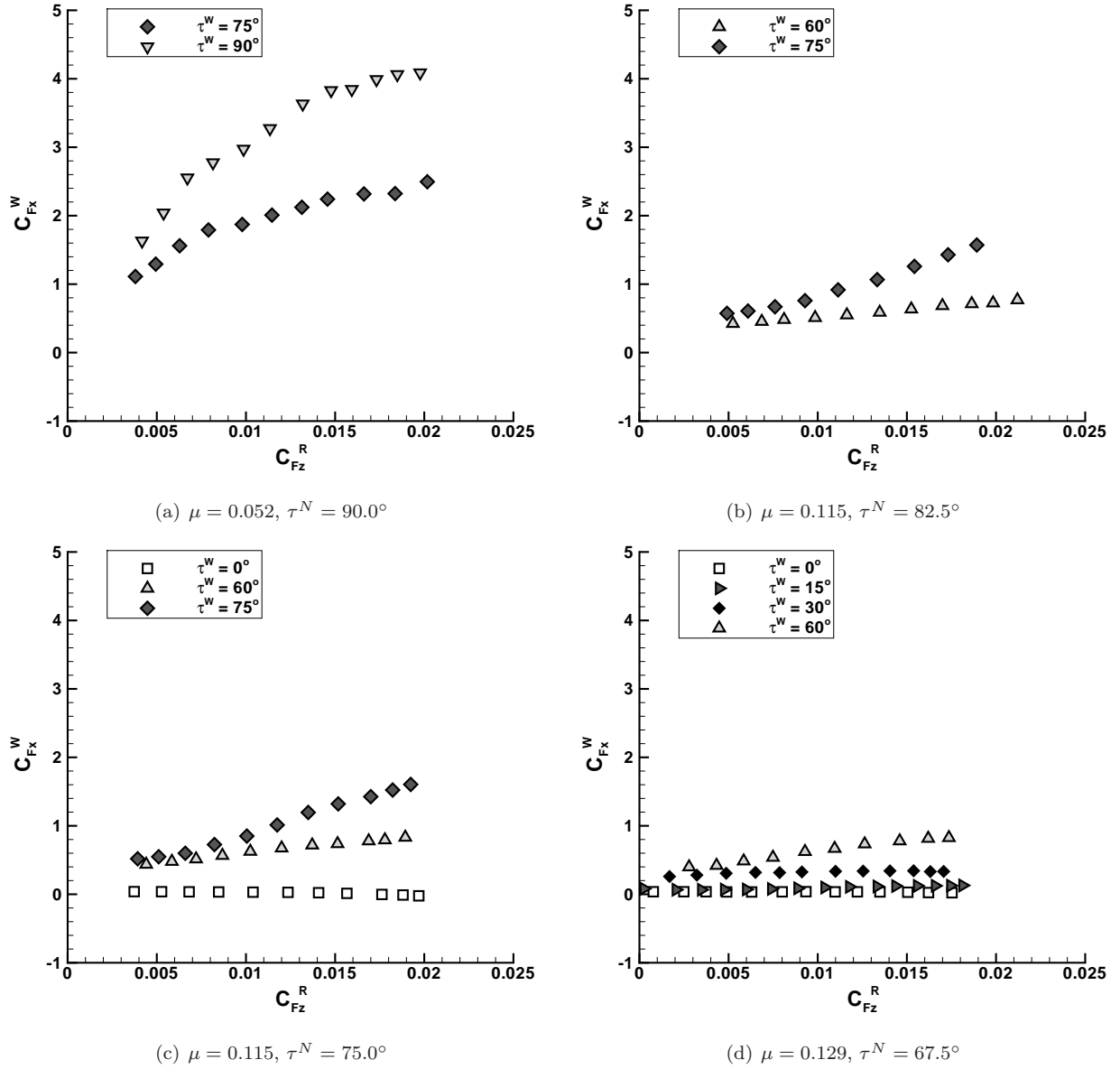
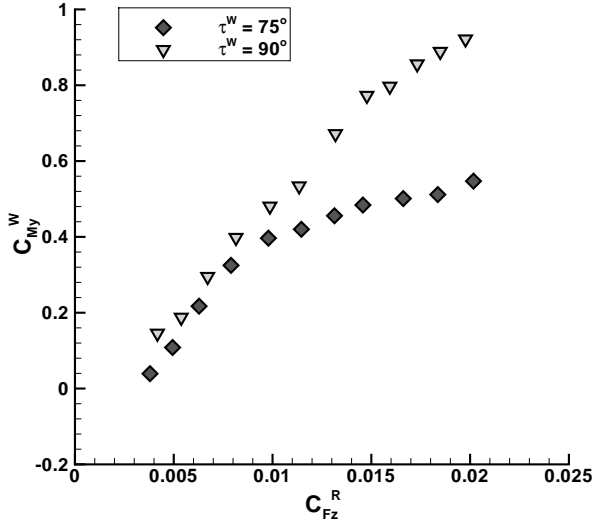
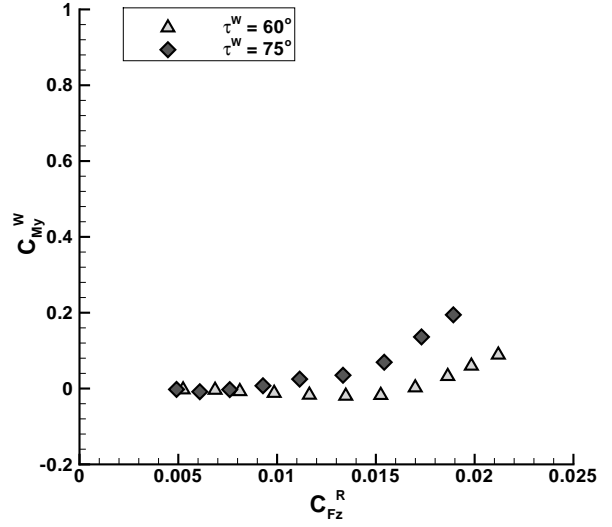


Figure 13: Wing longitudinal force coefficient  $C_{F_x}^W$  as function of rotor vertical force coefficient  $C_{F_z}^R$  for the half-span model configuration. Comparison between different tilting wing angle  $\tau^W$  for different advance ratios and nacelle angles.

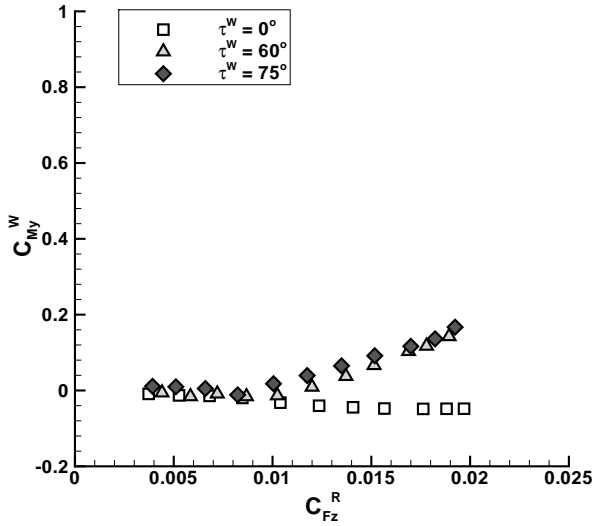
outer wing portion resulted from the combination of the free-stream velocity with the rotor slipstream. By comparing the two different wing configurations tested, small but non-negligible differences were observed on wing aerodynamic loads only for rotor vertical force values higher than 0.013. For instance, at  $C_{F_z}^R = 0.019$  the wing vertical force coefficient was 1.37 when the outer part of the wing was placed at  $75^\circ$  of incidence, while it was 1.14 when  $\tau^W$  was  $60^\circ$ . Moreover, at  $C_{F_z}^R = 0.019$  the longitudinal force measured when  $\tau^W = 75^\circ$  increased by 51 % with respect to the case having  $\tau^W$  equal  $60^\circ$ . In the same condition, the wing



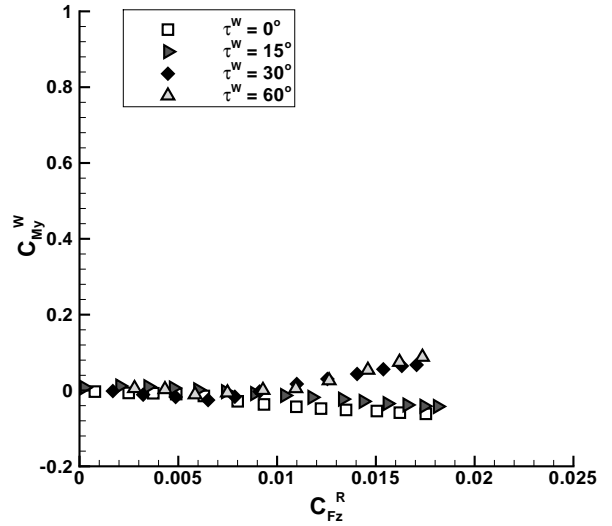
(a)  $\mu = 0.052, \tau^N = 90.0^\circ$



(b)  $\mu = 0.115, \tau^N = 82.5^\circ$



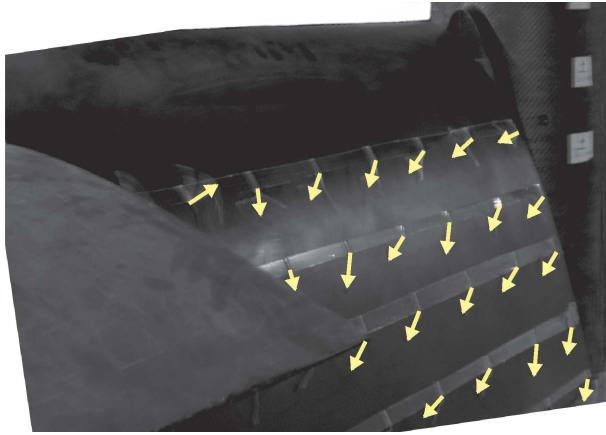
(c)  $\mu = 0.115, \tau^N = 75.0^\circ$



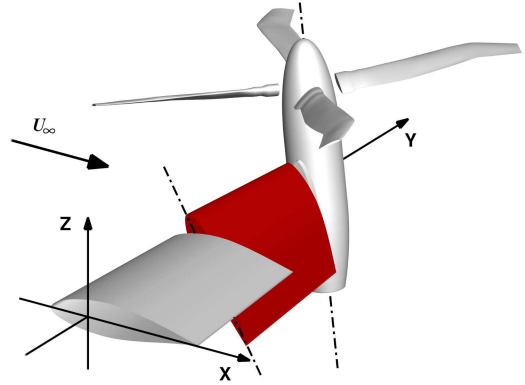
(d)  $\mu = 0.129, \tau^N = 67.5^\circ$

Figure 14: Wing pitching moment coefficient  $C_{My}^W$  as function of rotor vertical force coefficient  $C_{Fz}^R$  for the half-span model configuration. Comparison between different tilting wing angle  $\tau^W$  for different advance ratios and nacelle angles.

pitching moment for  $\tau^W = 75^\circ$  was approximately twice the pitching moment for  $\tau^W = 60^\circ$ . As shown in Figure 14(b), negative values of the pitching moment coefficient were found at low  $C_{Fz}^R$  for both wing configurations. Surface tufts were used to examine the flow on the upper surface of the wing. Figure 15 illustrates the tuft patterns on the tilting wing upper surface that have been sketched from moving videos which were recorded at the same rotor attitude for each wing configuration tested. Tuft patterns were not well defined in these instantaneous pictures since the camera exposition time was too long with respect



(a)  $\tau^W = 60^\circ$ ,  $C_{F_z}^R = 0.0191$



(b)  $\tau^W = 75^\circ$ ,  $C_{F_z}^R = 0.0189$

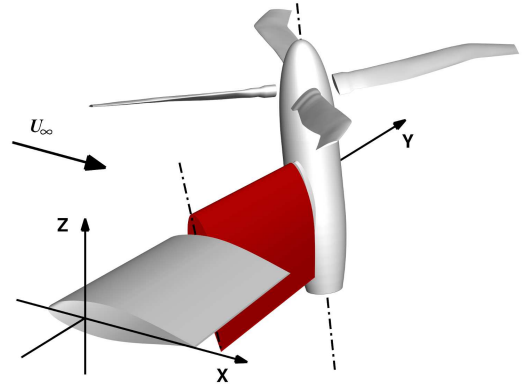


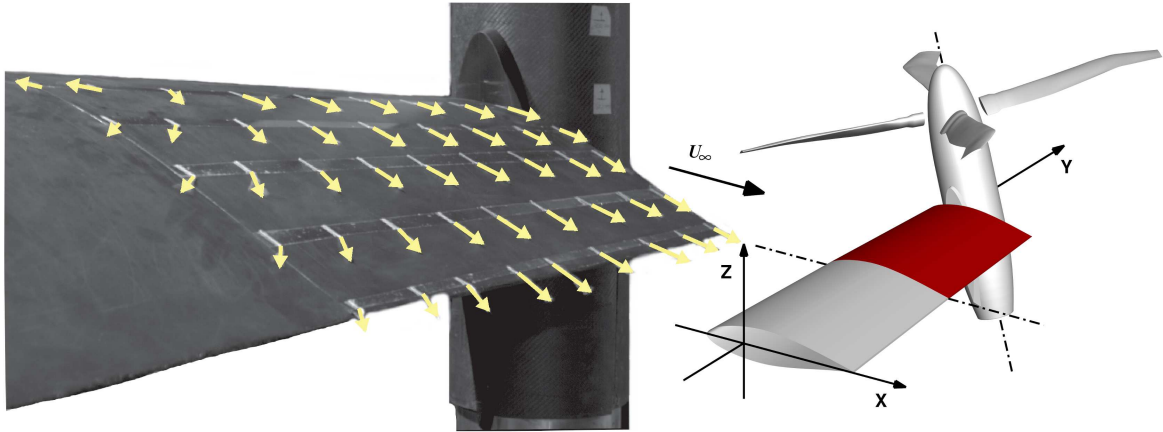
Figure 15: Tufts visualisations on the upper surface of the external part of the wing at different tilting wing angle  $\tau^W$ . Test condition:  $\tau^N = 82.5^\circ$ ,  $\mu = 0.115$ .

to the characteristic time of the tuft fluctuations. The arrows depicted in Figure 15 were drawn taking into account the maximum displacement of fluctuating tufts to highlight their mean positions. Thus, tuft patterns gave only an idea of the direction of the flow near the wing surface and did not indicate the velocity magnitude. Furthermore, tufts fluctuations revealed that the flow near the surface was characterised by a high level of unsteadiness. When looking at tufts' mean directions, a strong span-wise flow could be noted in both cases. However, when  $\tau^W$  was  $75^\circ$  (see Figure 15(b)) tufts appeared to be more deflected toward the fixed wing than for  $\tau^W = 60^\circ$  (see Figure 15(a)).

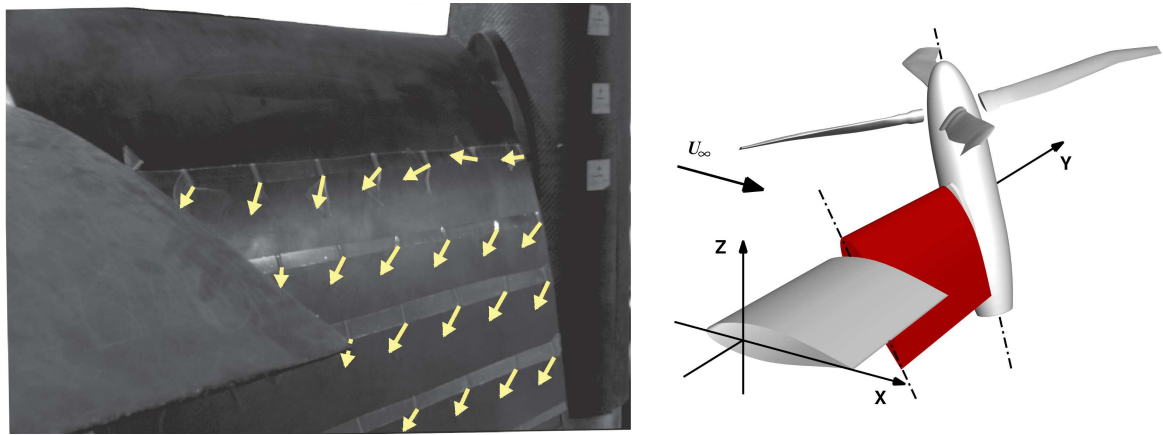
The tests at  $\mu = 0.115$  and  $\tau^N = 75^\circ$  were carried out using the same wing configurations already employed in the previous case, plus an additional configuration corresponding to the untilted wing case ( $\tau^W = 0^\circ$ ). As clearly shown in Figure 12(c), 13(c) and 14(c), high values of  $\tau^W$  produced high vertical

and longitudinal forces on the wing as well as high pitching moments. When  $\tau^W$  was set to  $75^\circ$  and  $60^\circ$  of incidence, the magnitude of the wing airloads increased as the rotor vertical force increased. In particular, the wing vertical force increased as the tilting wing geometrical angle of attack was decreased from  $75^\circ$  to  $60^\circ$  of incidence. For instance, at  $C_{F_z}^R = 0.019$  the resulting wing vertical force coefficient was 1.26 when  $\tau^W = 60^\circ$  and 1.12 when  $\tau^W = 75^\circ$ . Furthermore, when changing the tilting wing angle from  $75^\circ$  to  $60^\circ$  of incidence, the wing longitudinal force was reduced up to 47 % at  $C_{F_z}^R = 0.019$ , going from 1.57 to 0.83. On the other hand, rather different results were found when  $\tau^W = 0^\circ$ . The untilted wing configuration produced a negative vertical force of the order of 4 % of the actual rotor thrust, small longitudinal force and negative pitching moment. This result was in line with experimental data measured by Marr et al. [16] that observed a similar behaviour on the wing of the scaled Bell Model D-270 for low advance ratio. Such wind tunnel campaign demonstrated that the wing of a tiltrotor with conventional configuration begins to contribute to the lift of the whole aircraft when forward speed is higher than 18 m/s (corresponding in that case to an advance ratio of 0.14). For lower free stream velocities, Marr et al. observed that the wing subjected to the rotor wake still produced a negative vertical force, as in the hovering case. The examination of tufts visualisations on the upper surface of the tilting wing portion confirmed the results discussed in the airloads analysis. As shown in Figure 16, significant differences could be observed when comparing tufts patterns recorded for different configurations. Also in this case, the arrows were drawn to highlight tuft mean positions with respect to their maximum displacement. The untilted wing configuration presented a regular tufts distribution on all of the upper surface except for the region near the tilting section (see Figure 16(a)). In this region, the presence of span-wise flow revealed the blade tip vortex impinging on the upper surface of the wing. This phenomenon was responsible for producing negative vertical force on the wing, as already showed by balance data (see Figure 12(c)). Tufts visualisations at high tilting wing angles of attack presented high fluctuations and shown span-wise flow. However, tufts indicated flow separation on a wide region of the wing surface only at  $\tau^W = 75^\circ$  (see Figure 16(c)). The occurrence of flow separation on the outer wing portion confirmed the strong increase of the wing longitudinal force component with respect to the case having  $\tau^W = 60^\circ$ , as highlighted by airloads measurements (see Figure 13(c)).

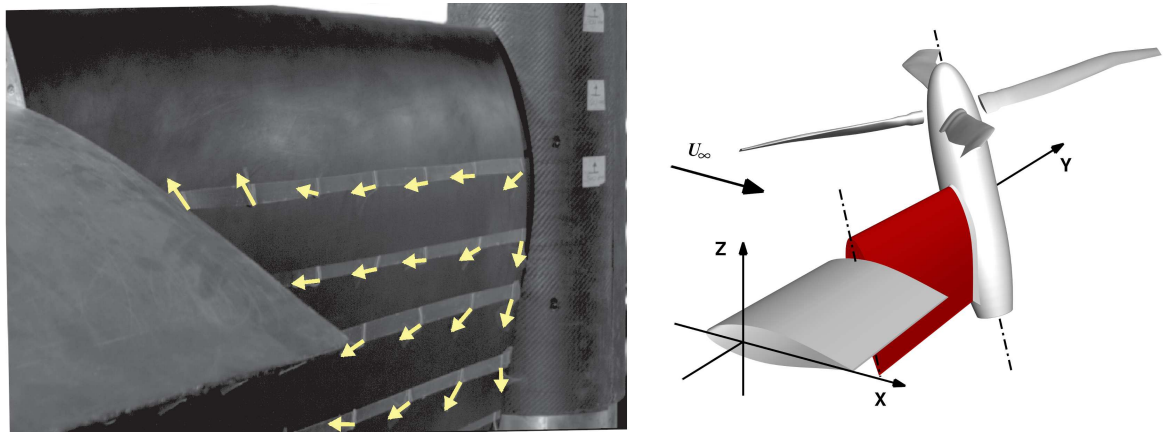
The fourth nacelle angle of attack considered during the measurements was  $\tau^N = 67.5^\circ$ . In this regard, Figure 12(d), 13(d) and 14(d) compare the wing aerodynamic performance measured for an advance ratio of 0.129 when the outer part of the wing was alternatively rotated at  $60^\circ$ ,  $30^\circ$ ,  $15^\circ$  and  $0^\circ$ . The former and the latter wing configurations showed a very similar behaviour with respect to the case with the nacelle at  $75^\circ$  of incidence. In particular, at  $60^\circ$  of incidence the wing exhibited good performance in terms of vertical and longitudinal force components reaching respectively a maximum value of 1.21 and 0.82 at  $C_{F_z}^R = 0.0175$ . On the other hand, when the tilting wing angle was placed at  $30^\circ$  and  $15^\circ$  of incidence, the wing still showed good lifting capabilities, as in the case with  $\tau^W = 60^\circ$  (see Figure 12(d)), producing smaller longitudinal forces, as in the case with  $\tau^W = 0^\circ$  (see Figure 13(d)). In such flight condition, the effect of the rotor wake



(a)  $\tau^W = 0^\circ$ ,  $C_{Fz}^R = 0.0185$



(b)  $\tau^W = 60^\circ$ ,  $C_{Fz}^R = 0.0177$



(c)  $\tau^W = 75^\circ$ ,  $C_{Fz}^R = 0.0179$

Figure 16: Tufts visualisations on the upper surface of the external part of the wing at different tilting wing angle  $\tau^W$ . Test condition:  $\tau^N = 75.0^\circ$ ,  $\mu = 0.115$ .

on the wing pitching moment is apparent from Figure 14(d). Indeed, the two intermediate wing configurations ( $\tau^W = 30^\circ$  and  $15^\circ$ ) led to pitching moment coefficients with opposite signs. This result suggested that the interaction mechanism between wing and rotor changed the load distribution on at least the tilting wing when it rotated from  $30^\circ$  to  $15^\circ$  of incidence.

### 3.3. Whole aircraft analysis

In order to discuss the effects of the wing/rotor aerodynamic interaction on the aircraft performance, the overall aircraft lifting capabilities and drag penalties are analysed in this section. The overall aircraft performance was estimated adding the contribution of the aircraft components not included in the wind tunnel model (nacelle, fuselage and both horizontal and vertical stabilisers) to the rotor and wing airloads obtained from the experiments. These contributions were approximately estimated using classical tools commonly employed in preliminary aircraft design. The nacelle aerodynamic force components were computed taking into account its frontal area, the velocity resulting from the combination of free-stream and rotor slipstream, and the actual angle of attack modified by the rotor wake. The effect of the rotor on the nacelle was estimated using the simple momentum theory in forward flight [38]. Since the tiltwing aircraft was characterised by small rotors placed at wing tips, the influence of rotors wakes on the fuselage was considered negligible, thus it was not taken into account for calculating the fuselage aerodynamic loads. The fuselage longitudinal force component was calculated applying a classical approach used in preliminary aircraft design [43], while its vertical force was reasonably assumed to be zero since only the aircraft condition at zero angle of attack and sideslip was considered in this study. For the same reason, the longitudinal force components produced by horizontal and vertical stabilisers were included in the fuselage drag evaluation [43] while their vertical force component was neglected.

Figure 17 shows the performance of the whole aircraft in three different phases of the conversion manoeuvre as function of rotor vertical force coefficient  $C_{F_z}^R$ . The wing configurations tested in each flight condition are compared in these pictures to highlight the effects of the wing/rotor interaction on the aircraft performance. Figure 17(a), 17(c) and 17(e) illustrate the aircraft lifting capabilities in terms of the ratio between the total vertical force component (given by  $F_z^R + F_z^W + F_z^N$ ) and the aircraft weight  $F_{Weight}^A$ . The horizontal dashed lines drawn in the pictures represent the vertical equilibrium condition (i.e. the aircraft lift equal to the aircraft weight). Such condition was never achieved during the experiments since the maximum thrust produced by the rotor was slightly lower than the one required to reach the equilibrium because of power limitations due to motor capacity. Nevertheless, the trend of the ratio between total vertical force component and the aircraft weight, as a function of the vertical force coefficient developed by the rotor, appears quite clear moving toward the aircraft trimmed flight conditions. Figure 17(b), 17(d) and 17(f) display the aircraft propulsive force variation as the total longitudinal force component (given by  $F_x^R + F_x^W + F_x^N + F_x^{FT}$ ) divided by the aircraft weight  $F_{Weight}^A$ . According to the aircraft reference

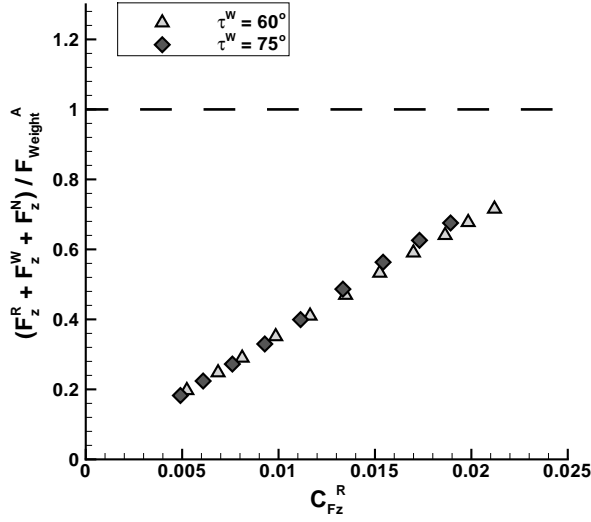
system (see Figure 4), a positive value of the longitudinal force component corresponded to a net drag force while a negative value corresponded to a propulsive force. The horizontal dashed lines reported in these figures indicate the longitudinal equilibrium condition in which the aircraft drag is counterbalanced by the propulsive force generated by the rotors.

In the first condition ( $\mu = 0.115$  and  $\tau^N = 82.5^\circ$ ) the remarkable differences in the wing lift coefficient observed for  $\tau^W = 75^\circ$  and  $60^\circ$  (see Figure 12(b)) did not produce considerable effects on the lifting capabilities of the whole aircraft, as depicted in Figure 17(a). However as illustrated in Figure 17(b), the wing configuration strongly influenced the aircraft longitudinal force component. Indeed, when  $\tau^W = 75^\circ$  the aircraft drag (equal to  $F_x^W + F_x^N + F_x^{FT}$ ) was always higher than the rotor propulsive force ( $F_x^R$ ) thus the resulting longitudinal force component assumed positive values, preventing the aircraft from flying in forward flight. On the contrary, when the tilting wing was set to an angle of  $60^\circ$ , the aircraft drag became lower than the rotor propulsive force for  $C_{F_z}^R$  values higher than 0.013. In such conditions the aircraft longitudinal force component corresponded to a propulsive force with negative values.

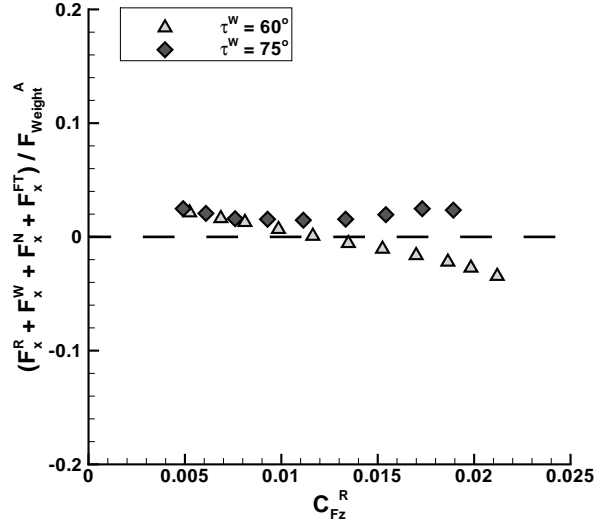
In the second analysed flight condition ( $\mu = 0.115$  and  $\tau^N = 75^\circ$ ), the effect of the tilting wing rotation on the aircraft lift is apparent by comparing the untilted wing case with the other configurations tested ( $\tau^W = 75^\circ$  and  $60^\circ$ ), as shown in Figure 17(c).

When the untilted wing configuration was employed, the aircraft lift was lower than the other cases since the wing produced a negative vertical force instead of a positive one (see Figure 12(c)). As a consequence, higher values of rotor thrust and power were needed to achieve the vertical equilibrium condition when  $\tau^W = 0^\circ$ . In this case the aircraft longitudinal force component was always negative, as illustrated in Figure 17(d), since the drag force produced by the untilted wing at zero angle of attack with respect to the free stream velocity was very small. The aircraft longitudinal force component corresponded to a propulsive force also when the outer part of the wing was placed at  $75^\circ$  and  $60^\circ$  of incidence. This condition was achieved for  $C_{F_z}^R$  values higher than 0.008 and 0.006 respectively. Nevertheless, the comparison between the three wing configurations tested (see Figure 17(d)) illustrates that the lower the tilting wing angle the higher the propulsive effect given by the rotor.

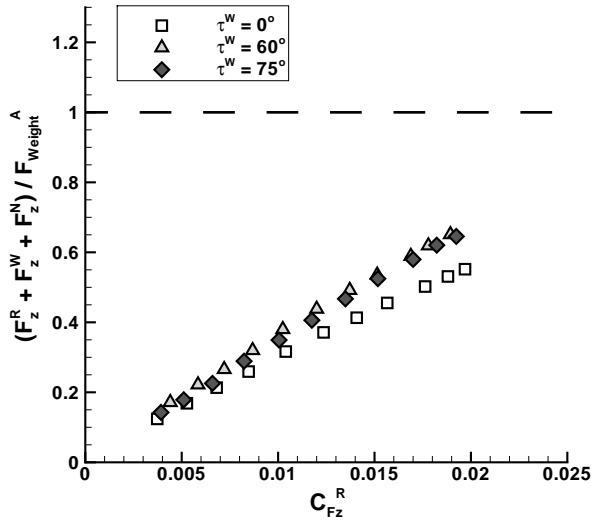
Similar results were found when the third flight condition was taken into account ( $\mu = 0.129$  and  $\tau^N = 67.5^\circ$ ). As expected, the untilted wing configuration provided very small lift (negative, see Figure 12(d)) and drag force components, allowing to obtain lower aircraft lift and higher propulsive force values with respect to the other wing configurations tested ( $\tau^W = 60^\circ, 30^\circ$  and  $15^\circ$ ). Oppositely to what was observed for the previous cases, the variations in the wing lift coefficient found for non-zero tilting wing configurations (see Figure 12(d)) yielded non-negligible differences in terms of aircraft lifting capabilities, since the rotor vertical force component  $F_z^R$  decreased as the nacelle angle of attack decreased. In particular, as depicted in Figure 17(e), the higher the tilting wing angle of attack, the higher the whole aircraft lift. Figure 17(f) illustrates that for  $C_{F_z}^R$  values higher than 0.006, the aircraft longitudinal force component



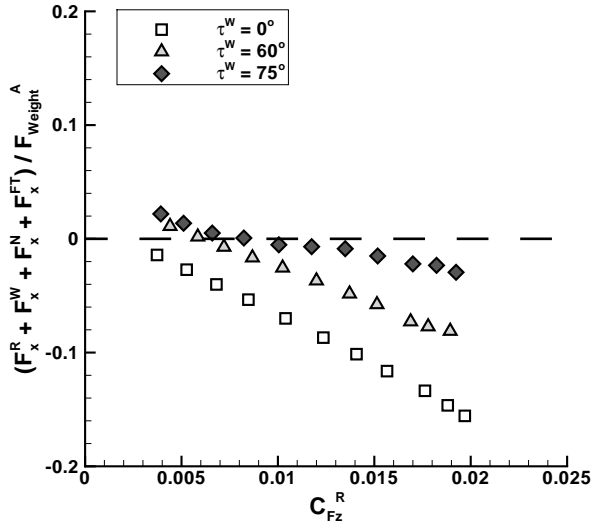
(a)  $\mu = 0.115, \tau^N = 82.5^\circ$



(b)  $\mu = 0.115, \tau^N = 82.5^\circ$



(c)  $\mu = 0.115, \tau^N = 75^\circ$

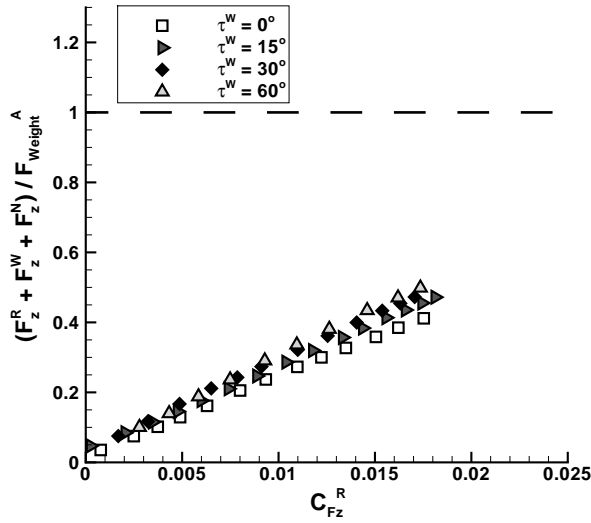


(d)  $\mu = 0.115, \tau^N = 75^\circ$

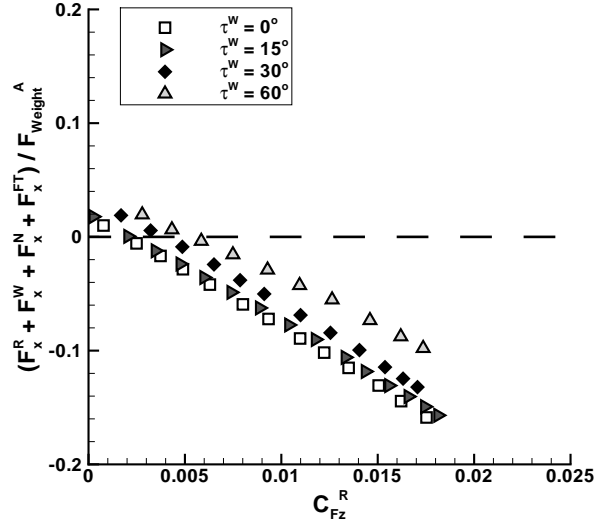
always corresponded to a propulsive force whatever the wing configuration adopted.

The present analysis showed that in the first part of the transition manoeuvre the whole aircraft performance strongly depended on the wing configuration and was influenced by the aerodynamic interaction between wing and rotor. Furthermore, the interaction mechanism varied as the aircraft configuration and the flight condition changed.

The experimental results showed that the tilting wing solution allowed to efficiently reduce the download generated by the rotor wake impinging on the wing. On the other hand, the rotation of the tilting wing produced high drag values as the wing angle of attack  $\tau^W$  increased. For some combinations of nacelle and



(e)  $\mu = 0.129, \tau^N = 67.5^\circ$



(f)  $\mu = 0.129, \tau^N = 67.5^\circ$

Figure 17: Aircraft performance as function of rotor vertical force coefficient  $C_{Fz}^R$ . Comparison between several wing configurations in three phases of the first part of the transition manoeuvre.

tilting wing angles of attack, the rotor propulsive effect was drastically reduced by the wing drag. In order to allow the aircraft to convert from helicopter to aeroplane mode (from hovering to cruise flight) the tilting wing angle had to be carefully adjusted during the manoeuvre: the aim was to look for a wing configuration that maximises the aircraft lifting capabilities while minimising the drag penalties. As a consequence, a proper wing configuration allowed the aircraft to perform the conversion manoeuvre using a reduced amount of rotor thrust and so requiring less power than a tiltrotor having a conventional wing layout. In conclusion, present results demonstrated that the possibility to rotate the outer wing independently of rotor and nacelle was essential to carry out the conversion, also confirming the reliability of the partially tilting wing solution employed for instance in the ERICA tiltrotor design.

#### 4. Conclusions

The performance of a tiltrotor aircraft employing the partially tilting wing solution was investigated during the first stage of the transition manoeuvre from helicopter to aeroplane flight mode within a comprehensive test campaign for aerodynamic loads measurements carried out in the wind tunnel test facility of Politecnico di Milano. The aircraft behaviour was analysed providing a detailed description of the effects related to the aerodynamic interaction between its wing and the rotor wake system in several flight conditions and nacelle/wing configurations.

The comparison between isolated rotor and half-span model airloads measurements revealed that in

forward flight conditions, rotor performance was not influenced by the presence of the wing or by its configuration. On the other hand, it was observed that the wing produced small effects on rotor kinematics, particularly on the longitudinal cyclic pitch control when high tilting wing angles of attack were used.

Experimental data demonstrated that wing airloads depended on the tilting wing configuration and they were strongly influenced by the aerodynamic interaction between wing and rotor. Such a mechanism was mainly controlled by the advance ratio and by the nacelle attitude. It affected the flow field behaviour around the tilting wing portion, as confirmed by tufts visualisations. Furthermore, the combination of free stream velocity and rotor slipstream resulted in a substantial modification of the actual angle of attack seen by the tilting wing sections. These effects allowed for a good aerodynamic performance of the wing (i.e. high lift and small drag forces) when proper tilting wing angles of attack were employed.

The analysis of the whole aircraft clearly illustrated the effectiveness of the partially tilting wing solution during the initial phases of the transition manoeuvre. Indeed, the independent rotation of the external part of the wing with respect to the nacelle rotation allowed the tiltwing to have good lifting capabilities and limited drag penalties in all the flight conditions experienced during the conversion. In particular, at the very beginning of the manoeuvre the comparison between different tilting wing angles showed that they produced different results in terms of propulsive force only, since the lift provided by the wing represented a small fraction of the aircraft lift. In the next steps, when the nacelle was further rotated by moving to the aeroplane mode, the comparison between several wing configurations revealed that the lower the tilting wing angle employed, the higher the rotor thrust required to achieve the vertical equilibrium condition and the propulsive force produced. As a consequence, higher values of power were needed to achieve the vertical equilibrium condition.

The present work provides a thorough experimental assessment of the performance of a tiltwing aircraft during the transition manoeuvre and represents an interesting database to be used for validating CFD, CSD and coupled CFD/CSD analyses, widely performed for the investigation of such aircraft configuration.

## References

- [1] R. Reber, Civil tiltrotor transportation for the 21<sup>st</sup> century, in: AIAA 93-4875, AIAA International powered lift conference, 1993.
- [2] M. Maisel, D. Giulianetti, D. Dugan, The history of the xv-15 tilt rotor research aircraft: from concept to flight, Monographs in Aerospace History, 17 SP-2000-4517, NASA History Division, Washington, D.C., USA (2000).
- [3] P. Dancik, F. Mazzitelli, W. Peck, Test experience on the vertol 76 vtol research aircraft, American Helicopter Society 14<sup>th</sup> Annual Forum, Washington, D.C., USA, 1958.
- [4] W. Johnson, G. Yamauchi, M. Watts, Designs and technology requirements for civil heavy lift rotorcraft, American Helicopter Society Vertical Lift Aircraft Design Conference, San Francisco, California, USA, 2006.
- [5] M. A. McVeigh, The v-22 tiltrotor large-scale rotor performance/wing download test and comparison with theory, Vertica 10 (3/4) (1986) 281-297.

- [6] T. L. Wood, M. A. Peryea, Reduction of tiltrotor download, *Journal of the American Helicopter Society* 40 (3) (1995) 42–51.
- [7] F. Felker, J. S. Light, Aerodynamic interactions between a rotor and wing in hover, *Journal of the American Helicopter Society* (1988) 53–61.
- [8] M. McCluer, J. Johnson, Full-span tiltrotor aeroacoustic model (fs tram). overview and initial testing, American Helicopter Society Aerodynamics, Acoustics, and Test and Evaluation Technical Specialists’ Meeting, San Francisco, CA, USA, 2002.
- [9] M. Potsdam, R. Strawn, Cfd simulations of tiltrotor configurations in hover, *Journal of the American Helicopter Society* 50 (1) (2005) 82–94.
- [10] W. Johnson, Calculation of the aerodynamic behavior of the tilt rotor aeroacoustic model (tram) in the dnw, *American Helicopter Society 57<sup>th</sup> Annual Forum*, Washington, D.C., USA, 2001.
- [11] T. Tai, Simulation and analysis of v-22 tiltrotor aircraft forward flight flowfield, in: *AIAA 95-0045, 33<sup>rd</sup> AIAA Aerospace Science Meeting & Exhibit*, Reno, NV, USA, 1995.
- [12] R. Funk, N. Komerath, Rotor wake interaction with a lifting surface, *American Helicopter Society 51<sup>st</sup> Annual Forum*, Fort Worth, TX, USA, 1995.
- [13] C. Matos, U. Reddy, N. Komerath, Rotor wake/fixed wing interactions with flap deflection, *American Helicopter Society 55<sup>th</sup> Annual Forum*, Montreal, Canada, 1999.
- [14] J. Magee, R. Taylor, F. McHugh, N. Miller, L. Delarm, Wind tunnel test of a powerd tiltrotor performance model, Tech. Rep. Technical Report AFFDL-TR-71-62, Volume V, Boeing Company, Vertol Division, Philadelphia, PA, USA (1971).
- [15] R. Marr, K. Sambell, G. Neal, V/stol tilt rotor study. volume 6: Hover, low speed and conversion tests of a tilt rotor aeroelastic model (model 300), Tech. Rep. NASA-CR-114615, Bell Helicopter Co., Fort Worth, TX, USA (1973).
- [16] R. Marr, D. Ford, S. Ferguson, Analysis of the wind tunnel test of a tilt rotor power force model, Tech. Rep. NASA-CR-137529, Bell Helicopter Co., Fort Worth, TX, USA (1974).
- [17] J. Weiberg, M. Maisel, Wind-tunnel tests of the xv-15 tilt rotor aircraft, Tech. Rep. TM 81177 (also AVRADCOM Technical Report TR-80-A-3), NASA, Ames Research Center, Moffett Field, CA, USA (1980).
- [18] L. Young, D. Lillie, M. McCluer, G. Yamauchi, M. Derby, Insights into airframe aerodynamics and rotor-on-wing interactions from a 0.25-scale tiltrotor wind tunnel model, *American Helicopter Society Aerodynamics, Acoustics, and Test and Evaluation Technical Specialists’ Meeting*, San Francisco, CA, USA, 2002.
- [19] P. Alli, F. Nannoni, M. Cicalè, Erica: The european tiltrotor design and critical technology projects, in: *AIAA/ICAS, International Air and Space Symposium and Exposition: The Next 100 Years*, Dayton, Ohio, USA, 2005.
- [20] P. Beaumier, J. Decours, T. Lefebvre, Aerodynamic and aeroacoustic design of modern tilt-rotors: the onera experience, *26<sup>th</sup> International Congress of the Aeronautical Sciences*, Anchorage, AK, USA, 2008.
- [21] G. Gibertini, F. Auteri, G. Campanardi, C. Macchi, A. Zanotti, A. Stabellini, Wind tunnel tests of a tilt-rotor aircraft, *The Aeronautical Journal* 115 (1167) (2011) 315–322.
- [22] J. Hakkaart, A. Stabellini, A. Verna, A. de Bruin, H.-J. Langer, O. Schneider, M. Przybilla, I. Philipsen, A. Ragazzi, A. H. W. Hojmakers, First nicetrip powered wind tunnel tests successfully completed in dnw-llf, *American Helicopter Society 70<sup>th</sup> Annual Forum*, Montréal, Canada, 2014.
- [23] F. Lebrun, D. Munier, J. Decours, P. Beaumier, Onera s1ma wind tunnel testing capabilities of a modern tilt rotor, *American Helicopter Society 71<sup>th</sup> Annual Forum*, Virginia Beach, VA, USA, 2015.
- [24] G. Droandi, Wing-rotor aerodynamic interaction in tiltrotor aircraft, Ph.D. thesis, Politecnico di Milano, Milano, Italy (2014).
- [25] G. Droandi, G. Gibertini, Aerodynamic shape optimisation of a proprotor and its validation by means of cfd and experiments, *Aeronautical Journal* 119 (1220) (2015) 1223–1251.
- [26] G. Droandi, G. Gibertini, M. Lanz, G. Campanardi, D. Grassi, Wing-rotor interaction on a 1/4-scale tiltrotor half-model,

- 39<sup>th</sup> European Rotorcraft Forum, Moscow, Russia, 2013.
- [27] G. Droandi, A. Zanotti, G. Gibertini, D. Grassi, G. Campanardi, Experimental investigation of the rotor–wing aerodynamic interaction in a tiltwing aircraft in hover, *The Aeronautical Journal* 119 (1215) (2015) 591–612.
- [28] G. Droandi, G. Gibertini, A. Zanotti, Aerodynamic interaction between rotor and tiltable wing in hovering flight condition, *Journal of the American Helicopter Society* 60 (4) (2015) 1–20.
- [29] Droandi, G. Gibertini, Aerodynamic blade design with multi-objective optimization for a tiltrotor aircraft, *Aircraft Engineering and Aerospace Technology* 87 (1) (2015) 19–29.
- [30] W.H. Reed III, Propeller-rotor whirl flutter: A state-of-the-art review, *Journal of Sound and Vibration* 4 (3) (1966) 530–544.
- [31] D. Polak, W. Rehm, A. George, Effects of an image plane on the tiltrotor fountain flow, *Journal of American Helicopter Society* 45 (2) (2000) 90–96.
- [32] A. Darabi, A. Stalker, M. McVeigh, I. Wygnanski, The rotor wake above a tiltrotor airplane–model in hover, 33<sup>rd</sup> AIAA Fluid Dynamics Conference, Orlando, FL, USA, 2003.
- [33] F. Felker, Wing download results from a test of a 0.658-scale v-22 rotor and wing, *Journal of the American Helicopter Society* 37 (4) (1992) 58–63.
- [34] J. Barlow, W. Rae, A. Pope, *Low-Speed Wind Tunnel Testing*, John Wiley & Sons, INC, New York, NY, USA, 1999.
- [35] T. Strand, E. Levinsky, Wind tunnel tests of a free-wing tilt-propeller v/stol airplane model, Tech. Rep. AFFDL-TR-69-80, Defense Technical Information Center (1969).
- [36] D. Snyder, The quad tiltrotor: Its beginning and evolution, *International Powered Lift Conference*, Arlington, Virginia, USA, 2000.
- [37] W. Johnson, *Helicopter Theory*, Princeton University Press, Princeton, New Jersey, USA, 1980.
- [38] J. G. Leishman, *Principles of Helicopter Aerodynamics*, Cambridge Aerospace Series, New York, NY 10013–2473, USA, 2006.
- [39] H. Heyson, Wind-tunnel testing of vstol and stol aircraft, Tech. Rep. TM 78750, NASA, Langley Research Center, Hampton, VA, USA (1978).
- [40] M. Biava, G. Vigevano, Computational assessment of wind tunnel flow in closed and open section model rotor tests, *Journal of the American Helicopter Society* 59 (1) (2014) 1–17.
- [41] G. Leishman, A. Bagai, Fundamental studies of rotor wakes in low speed forward flight using wide-field shadowgraphy, in: AIAA-91-3232, 1<sup>st</sup> AIAA Applied Aerodynamics Conference, Baltimore, MD, USA, 1991.
- [42] S. Hoerner, *Fluid-Dynamic Drag. Theoretical, experimental and statistical information*, Hoerner Fluid Dynamics, Bakersfield, CA, USA, 1965.
- [43] J. Roskam, *Aircraft design*, Roskam Aviation and Engineering Corporation, Rt4, Box 274, Ottawa, Kansas, 66067, USA, 1985.